The Wavenumber-One Instability and Trochoidal Motion of Hurricane-like Vortices

DAVID S. NOLAN AND MICHAEL T. MONTGOMERY

Department of Atmospheric Science, Colorado State University, Fort Collins, Colorado

LEWIS D. GRASSO

Cooperative Institute for Research in the Atmosphere, Fort Collins, Colorado

(Manuscript received 25 October 2000, in final form 9 May 2001)

ABSTRACT

In a previous paper, the authors discussed the dynamics of an instability that occurs in inviscid, axisymmetric, two-dimensional vortices possessing a low-vorticity core surrounded by a high-vorticity annulus. Hurricanes, with their low-vorticity cores (the eye of the storm), are naturally occurring examples of such vortices. The instability is for asymmetric perturbations of azimuthal wavenumber-one about the vortex, and grows in amplitude as $t^{1/2}$ for long times, despite the fact that there can be no exponentially growing wavenumber-one instabilities in inviscid, two-dimensional vortices. This instability is further studied in three fluid flow models: with high-resolution numerical simulations of two-dimensional flow, for linearized perturbations in an equivalent shallow-water vortex, and in a three-dimensional, baroclinic, hurricane-like vortex simulated with a high-resolution mesoscale numerical model.

The instability is found to be robust in all of these physical models. Interestingly, the algebraic instability becomes an exponential instability in the shallow-water vortex, though the structures of the algebraic and exponential modes are nearly identical. In the three-dimensional baroclinic vortex, the instability quickly leads to substantial inner-core vorticity redistribution and mixing. The instability is associated with a displacement of the vortex center (as defined by either minimum pressure or streamfunction) that rotates around the vortex core, and thus offers a physical mechanism for the persistent, small-amplitude trochoidal wobble often observed in hurricane tracks. The instability also indicates that inner-core vorticity mixing will always occur in such vortices, even when the more familiar higher-wavenumber barotropic instabilities are not supported.

1. Introduction

In certain experimental apparatuses, the equations of motion describing the dynamics of electron plasmas guided by a magnetic field are identical to the equations of motion for inviscid, incompressible fluid flow in two dimensions. This remarkable equivalence allows experimental physicists to simulate two-dimensional fluid flow in the laboratory, at Reynolds numbers many orders of magnitude higher than can be simulated accurately with numerical models or with actual fluids. A number of such experiments have provided insight into (nearly) inviscid two-dimensional vortex dynamics (Driscoll 1990; Huang et al. 1995; Driscoll et al. 1996; Schecter et al. 1999). In the context of this work, Smith and Rosenbluth (1990; hereafter SR) found an exact solution, in terms of quadratures, describing the evolution of azimuthal wavenumber-one perturbations to inviscid vortices. Furthermore, the long-time asymptotic limit of this solution predicts the appearance of an algebraically growing instability (streamfunction amplitudes growing like $t^{1/2}$ for long times) for any vortex that possesses an angular velocity maximum other than at the center axis.

Moderate to intense hurricanes, with their low-vorticity centers (the eye), are naturally occurring examples of vortices with angular velocity maxima away from their center axis. [While observationally obtained vorticity profiles have only recently been available—e.g., Reasor et al. (2000); or Kossin and Eastin (2001)—an angular velocity maximum can be inferred from any velocity profile which is concave up, or ''U-shaped,'' near the center, and many such profiles have been presented, e.g., Shea and Gray (1973, Fig. 3).] Furthermore, the close relationship between wavenumber-one perturbations and vortex motion indicates the importance of wavenumber-one instabilities (Willoughby 1992; Smith and Weber 1993; Reznik and Dewar 1994; Montgomery et al. 1999). To determine whether or not the SR instability could be significant in tropical cyclone dynamics, Nolan and Montgomery (2000a; hereafter NM) investigated its dynamics in two-dimensional vortices with dimensional scales similar to those of a weak tropical

Corresponding author address: Dr. David S. Nolan, GFDL/NOAA, P.O. Box 308, Princeton, NJ 08542.
E-mail: dsn@gfdl.noaa.gov

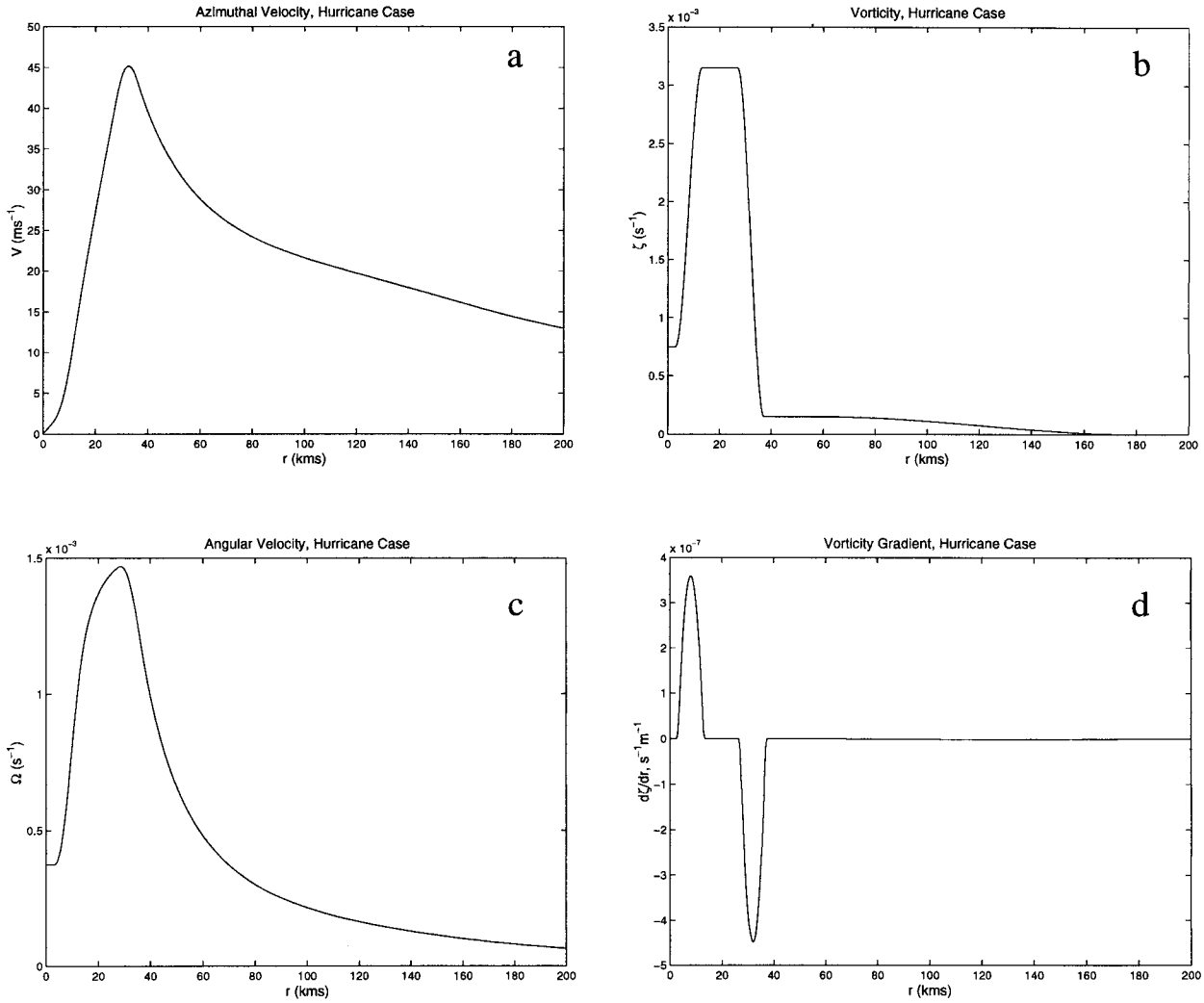

FIG. 1. Basic-state profiles for the Nolan and Montgomery (2000a) stable, hurricane-like vortex: (a) velocity, (b) vorticity, (c) angular velocity, and (d) vorticity gradient.

storm and a medium strength hurricane. Since NM wished to observe only the algebraic wavenumber-one instability, both the tropical storm and hurricane-like vortices were carefully constructed to be stable to exponentially growing, two-dimensional disturbances for all azimuthal wavenumbers. This was achieved in part through trial and error, using as a guide the stability analyses of Schubert et al. (1999) for two-dimensional vortices with stair-step vorticity profiles. The velocity, vorticity, vorticity gradient, and angular velocity profiles of the NM hurricane-like vortex are shown in Fig. 1. This vortex and modifications of it are used throughout the rest of this paper.

Nolan and Montgomery found that the instability does indeed have significant growth rates in hurricane-like vortices. Since the streamfunction and vorticity perturbation amplitudes grow as $t^{1/2}$, the perturbation kinetic energy grows linearly in time, and NM found that a wavenumber-one perturbation in the hurricane-like vortex could increase 20 times in energy within 24 h. (As SR showed, the growth rate of the algebraic instability depends both on the shape of the angular velocity profile and the structure of the initial perturbation, so one cannot make general statements about the growth rate of the instability.) Nolan and Montgomery further clarified a number of very interesting properties of the SR algebraic instability.

1) The solution can be divided into three parts: (i) a growing mode whose perturbation vorticity is exactly proportional to the basic-state vorticity gradient up to the radius of the maximum angular velocity (referred to hereafter as the RMΩ), but is zero beyond that point, and whose contribution to the total streamfunction grows as $t^{1/2}$; (ii) an excitation of a neutral mode, which represents a displacement of the entire vortex (a.k.a the ''pseudo-mode''); and (iii) a collection of sheared disturbances whose associated streamfunction decays as $t^{-1/2}$.

2) The instability can only be excited by initial conditions with vorticity inside the RMΩ. Perturbations whose vorticity is entirely outside the RMΩ will not result in instability.
3) Furthermore, algebraic growth will not result if the initial perturbation is exactly proportional to the growing part of the asymptotic solution. The ''growing part'' of the solution is in fact, by itself, a neutral mode. This is shown in the appendix of this paper.
4) The algebraic growth occurs due to an interaction, via the basic-state vorticity gradient, between this neutral mode and the disturbances whose associated streamfunction decays as $t^{-1/2}$. These disturbances are in fact a collection of sheared vortex-Rossby waves that are trapped in the vicinity of the vortex core by the angular velocity maximum (hereafter, $\overline{\Omega}_{\max}$), and their slow decay is due to their diminished shearing in the vicinity of $\overline{\Omega}_{\max}$.
5) The instability represents an oscillating displacement of the low-vorticity core of the vortex relative to the surrounding flow, that is, a wobble of the eye of the storm.

It is this last property of the algebraic instability that makes it clearly relevant to the known behaviors of tropical cyclones. The tracks of such storms often show a substantial oscillation, or wobble, with respect to some time-averaged motion vector, referred to as the *trochoidal motion* of the storm center. Such behavior has been documented in a number of observational studies dating back to the early use of radar to determine storm centers (Jordan and Stowell 1955; Jordan 1966) and was also identified in satellite images (Lawrence and Mayfield 1977). The trochoidal motion of the center has since been often observed in studies of the inner cores of hurricanes (Willoughby et al. 1984; Muramatsu 1986; Griffin et al. 1992; Roux and Viltard 1995), and is also seen in numerical simulations (Jones 1977; Abe 1987; Liu et al. 1999). The amplitude of the trochoidal oscillation can be quite small, so as to be lost in the temporal smoothing process that is used to produce ''best track'' records of tropical cyclones. An example of the trochoidal oscillation is shown in Fig. 2, which shows the motion of Hurricane Carla (1961) as deduced from radar observations and also its best track path (taken from Jarvinen et al. 1984).

A number of previous studies have addressed the oscillation of a tropical cyclone's path about its mean motion vector. Yeh (1950) and Kuo (1950, 1969) used classical hydrodynamics to treat such storms as isolated, barotropic vortices interacting with the mean flow and planetary rotation of the surrounding environment. In addition to the well-known rightward deflection of cyclonic vortices relative to the environmental flow, their solutions predicted trochoidal motion.[1] Flatau and Stevens (1993) predicted that wavenumber-one instabilities in a hurricane's outflow layer would cause trochoidal motion. Vertical shear in the environment has also been linked to storm motion. When the vortex is barotropic, vertical shear leads to a perturbation vorticity structure which can be interpreted as two like-signed potential vorticity (PV) anomalies, one at the surface and one near the tropopause, which are slightly displaced from one another. The PV anomalies tend to corotate, leading to trochoidal motion of the low-level center (Jones 1995; Reasor and Montgomery 2001). When the vortex is baroclinic, the upper and lower PV anomalies are of opposite sign, and instead induce propagation rather than corotation (Wu and Emanuel 1993; Flatau et al. 1994). For a realistic vertical structure, the impact of vertical shear would likely be a combination of these two effects.

The hurricane track motions discussed in these studies, while consistent with the general meandering motion observed in virtually all tropical cyclones, are fundamentally different in a number of ways from the wavenumber-one instability and trochoidal motion presented in this paper. For the most part, the trochoidal motions discussed in these previous studies are of substantially longer time scales

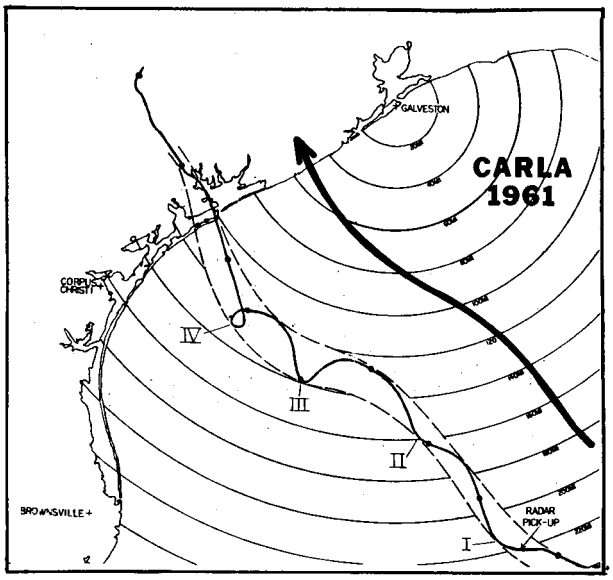

FIG. 2. The path of Hurricane Carla (1961) as reanalyzed by Jarvinen et al. (1984), showing four trochoidal oscillations just before landfall. Also shown (thick line) is the ''best track path,'' displaced northward for comparison. The range markers are at 20 n mi intervals. Original figure was adapted from *Weatherwise*, Oct 1961.

[1] The trochoidal motions predicted by Yeh (1950) and Kuo (1950, 1969) are not in fact necessary consequences of the vortex-environment interaction. Rather, they are a function of the initial conditions. Trochoidal motion is predicted only when the initial vortex motion is different from the environmental flow, much like the inertial motions of a particle disturbed on an f plane.

(12–48 h), and substantially larger distance scales (20–200 km) than the trochoidal motion of Hurricane Carla demonstrated in Fig. 2 or predicted in NM. Second, with the possible exception of the barotropic instability discussed by Flatau and Stevens (1993), these large-scale oscillations are a side effect of the hurricane's interaction with its environment, rather than fundamental to the vortex itself. Last, the wavenumber-one instability discussed by NM represents a displacement of the low-vorticity core *relative* to the surrounding eyewall structure, while the previous papers describe trochoidal motions of the *entire* hurricane vortex.

Preliminary nonlinear simulations of the instability by NM using a semispectral model showed that the continued growth of the instability ultimately leads to inner-core vorticity redistribution so as to remove the vorticity deficit from the center of the vortex, and perhaps ultimately to a complete redistribution of the vorticity into a nearly axisymmetric profile which decreases monotonically from the center. This is yet another way in which the present wavenumber-one dynamics are different from those reviewed above. When eyewall vorticity is mixed into the eye, the azimuthal wind profile is modified from that of a ''hollow vortex'' or ''stagnant core'' toward a profile with solid-body rotation at the center. From purely kinematic effects, this results in a lowering of the central pressure in the vortex. Emanuel (1997) has suggested that such inner-core vorticity mixing is necessary for a tropical cyclone to reach its maximum intensity (MPI), because this lowering of the central pressure increases the equivalent potential temperature (θ_e) of the air at the surface, essentially resulting in more heat being transferred from the ocean to the atmosphere. Inner-core asymmetries and the mixing associated with them have become more frequently observed due to the ever increasing resolution of both observational methods (Reasor et al. 2000; Kossin and Eastin 2001; Daida and Barnes 2000) and numerical simulations (Liu et al. 1997, 1999; Braun and Tao 2000; Braun et al. 2000; Fulton et al. 2000). As the wavenumber-one instability may play a role in the redistribution of vorticity in the eye and eyewall regions and thus also in intensity changes, it is important to develop a basic understanding of its dynamics.

In this paper, we present the results of further analyses of the wavenumber-one instability in a number of different fluid flow models. In section 2, the nonlinear dynamics of the instability in purely two-dimensional flow is further studied with high-resolution, low-viscosity simulations. In section 3, the behavior and dynamics of wavenumber-one perturbations are examined in an equivalent vortex in a shallow-water fluid. In section 4, the wavenumber-one instability is studied using the dynamical core of a mesoscale numerical model (RAMS, see section 4a) to simulate the evolution of a three-dimensional, balanced vortex whose wind field is modeled after a mature hurricane. The cumulative result of these investigations is that the wavenumber-one instability occurs in all types of vortices with low-vorticity cores, and is likely an important aspect of the inner-core dynamics of tropical cyclones.

2. High-resolution simulations in two dimensions

a. The model

Nolan and Montgomery found that the algebraic wavenumber-one instability was very sensitive to the presence of viscous dissipation. This implies that very high resolution is necessary to capture the long-term growth of the instability in a fully nonlinear model. It would also be ideal to simulate the instability in a very large domain, so as to limit or eliminate any boundary effects. For these reasons, we use a numerical model of incompressible two-dimensional fluid flow that has the special feature of adaptive mesh refinement (AMR). AMR provides for the utilization of an arbitrary number of refined, two-way nested grids. Furthermore, these grids are not necessarily fixed in time but rather can be moved and generated spontaneously by the model as determined by some arbitrary refinement criterion; however, in all the simulations presented here, the refinement boxes are essentially stationary. The model is based on a velocity-pressure formulation of the equations, is second-order accurate in space and time, and uses flux limiters to prevent the generation of spurious oscillations. Further presentations and discussions of the model are available in Almgren et al. (1998) and Nolan et al. (2000).

b. Initial conditions

The model domain is the square region within -400 km $\leq x, y \leq 400$ km. The velocity profile of the original NM vortex is modified so that its velocity field goes to zero at some finite radius, well within the confines of the model domain. This is achieved by multiplying the original velocity profile by a suitable exponentially decaying factor; that is,

$$\overline{V}^*(r) = \overline{V}(r) \exp\left[-\left(\frac{r}{r_c}\right)^8\right] \tag{2.1}$$

where for the simulations here we use $r_c = 250$ km. The resulting modified velocity and vorticity profiles are shown in Fig. 3.[2] As an initial perturbation to the basic-state vortex, we use the same wavenumber-one perturbation used throughout NM:

[2] Following the suggestion of a reviewer, we examined the stability of this vortex using the same methodology described in NM. It turns out that forcing the velocity profile to go to 0 near $r = 300$ km causes the appearance of unstable modes for wavenumbers $n = 2$, 3, and 4. These unstable modes are due to interactions between the inner and outer vorticity regions, and appear analogous to the ''type 2'' instabilities discussed by Kossin et al. (2000). However, the growth rates of these modes are relatively slow, with *e*-folding times of 12 h or more.

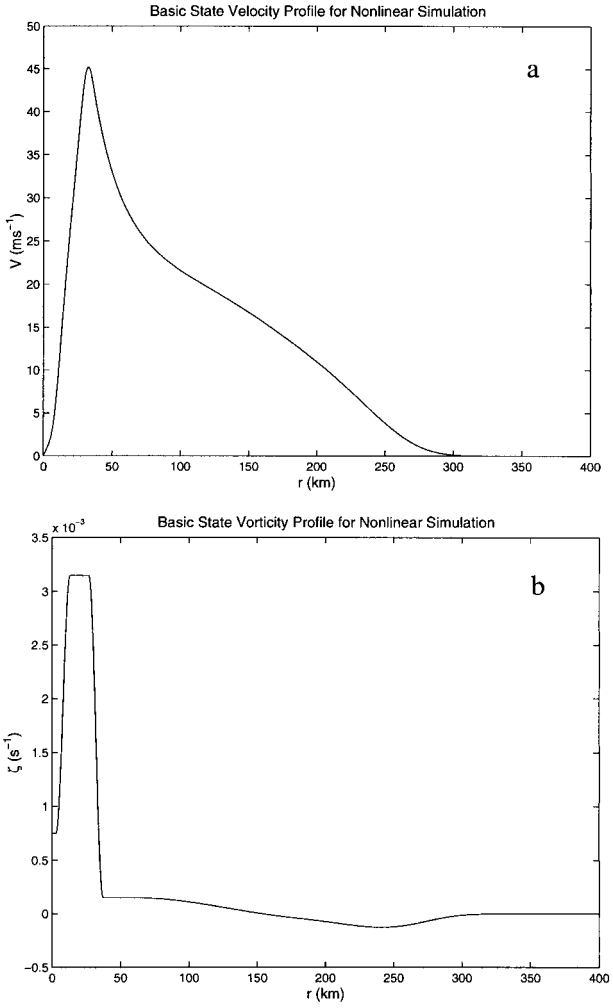

FIG. 3. Basic-state velocity (a) and vorticity (b) profiles for the two-dimensional nonlinear simulations.

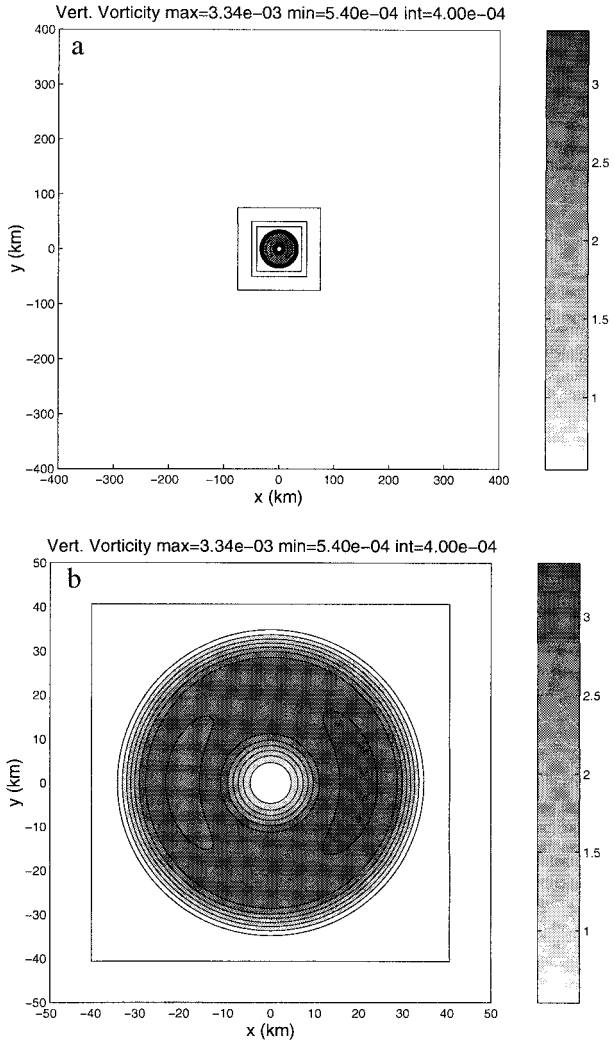

FIG. 4. Shaded contour plot of the initial vorticity field for the nonlinear simulations. The locations of the refinement grids are also shown, for (a) the entire domain, and (b) a close-up of the inner-core vorticity. Vorticity units: s^{-1}. This initial condition was used for all the simulations.

$$\zeta_1(r, t = 0) = A \exp\left[-\left(\frac{r - r_{\text{eye}}}{w_{\text{eye}}/4}\right)^2\right], \qquad (2.2)$$

where $r_{\text{eye}} = 20$ km is the center of the eyewall region, $w_{\text{eye}} = 24$ km is the width of the eye-wall region, and the maximum initial amplitude of the perturbation is 10% of the local basic state flow vorticity

$$A = 0.1 \times \overline{\zeta}(r_{\text{eye}}). \qquad (2.3)$$

The simulations presented here use a base grid with 128×128 grid points, such that the base grid spacing is 6.25 km. The simulation also uses three levels of refinement. The first two levels have factors of 2 decreases in the grid spacing, while the third level has a factor of 4 decrease in grid spacing, such that the grid spacing on the innermost grid is 390.625 m. The initial vorticity field, along with the locations of the refinement boxes at $t = 0$, is shown in Fig. 4. The criterion used to determine the locations of the refined grids is that the vorticity difference across any two grid points be no greater than 1% of the value of the average vorticity in the eyewall region. This requirement may not always be met within the innermost grid, since the number of refinement boxes is limited to three in these simulations.

c. Results

We performed four simulations of the instability, varying only the viscosity for each simulation, with values of $\nu = 10$, 20, 40, and 80 $m^2\ s^{-1}$. For short times, the evolution of the vortex was nearly identical for all values of ν, and the early evolution of the vortex with $\nu = 40\ m^2\ s^{-1}$ is shown every 20 min from $t = 2$ h to $t = 3$ h 40 min in Fig. 5. As expected, the initial perturbation results in a steadily growing wobble of the low-vorticity core. Associated with this wobble is a sim-

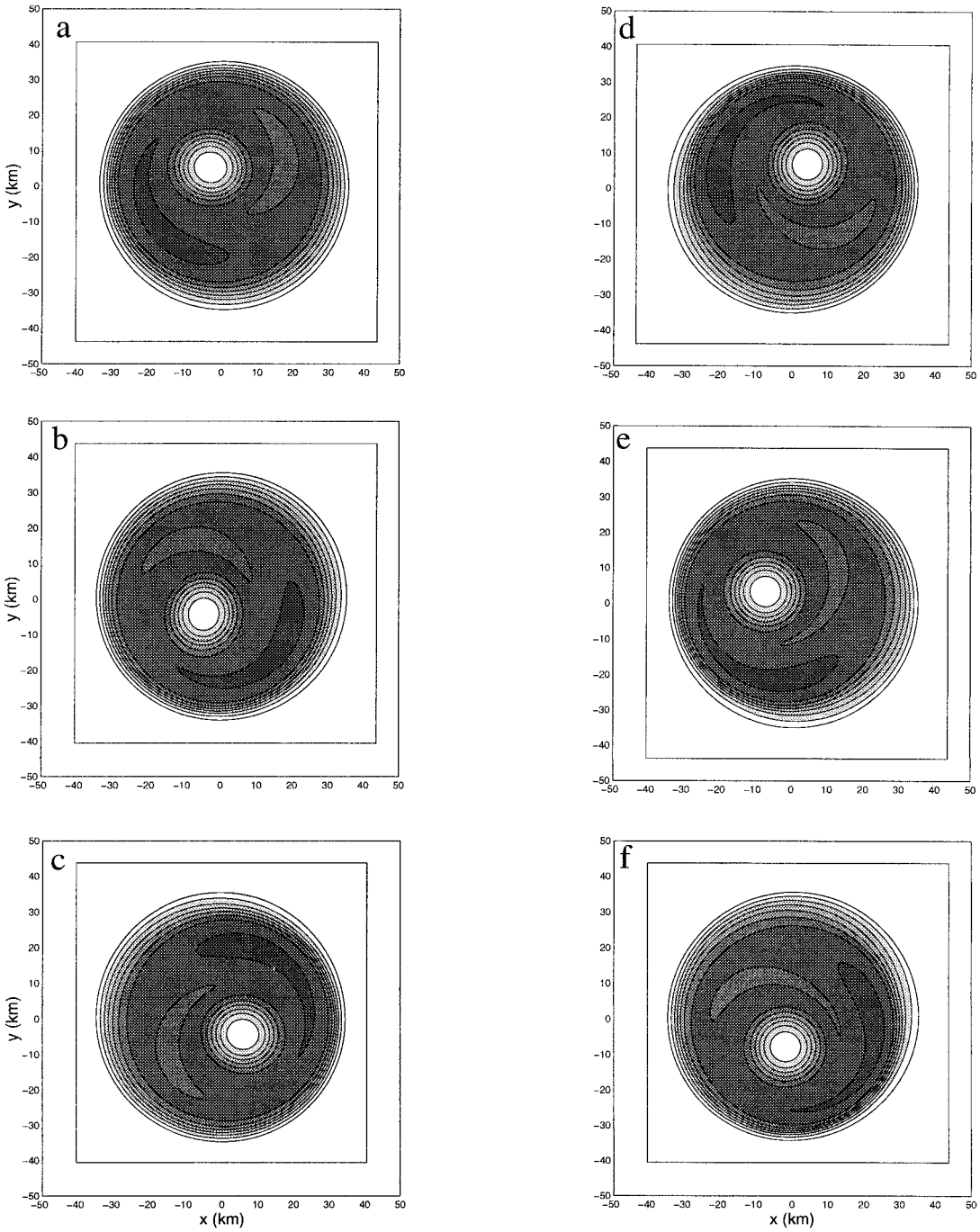

FIG. 5. Vertical vorticity fields in the inner core of the fully nonlinear simulation with $\nu = 40$ m^2 s^{-1} at (a) 120, (b) 140, (c) 160, (d) 180, (e) 200, and (f) 220 min. Units of vorticity: s^{-1}. Contour levels and shading are as in Fig. 4.

ilar wobble in the location of the center of the vortex as defined by both the minima of the streamfunction and pressure fields. The x coordinates of these minima are shown as functions of time in Fig. 6. It is perhaps confusing to see that the amplitude of the wobble only grows for a few hours and then begins to decay with time. This is not due to a decline of the algebraic instability mechanism, but rather is a feature of the nonlinear dynamics of the instability. As time evolves the low-vorticity core moves outward from the center not simply as a growing wavenumber-one perturbation, but rather as a coherent ''vortex hole,'' as is evident from Fig. 5. The vorticity at the vortex center is replaced by higher vorticity from the eyewall region, and the stream-

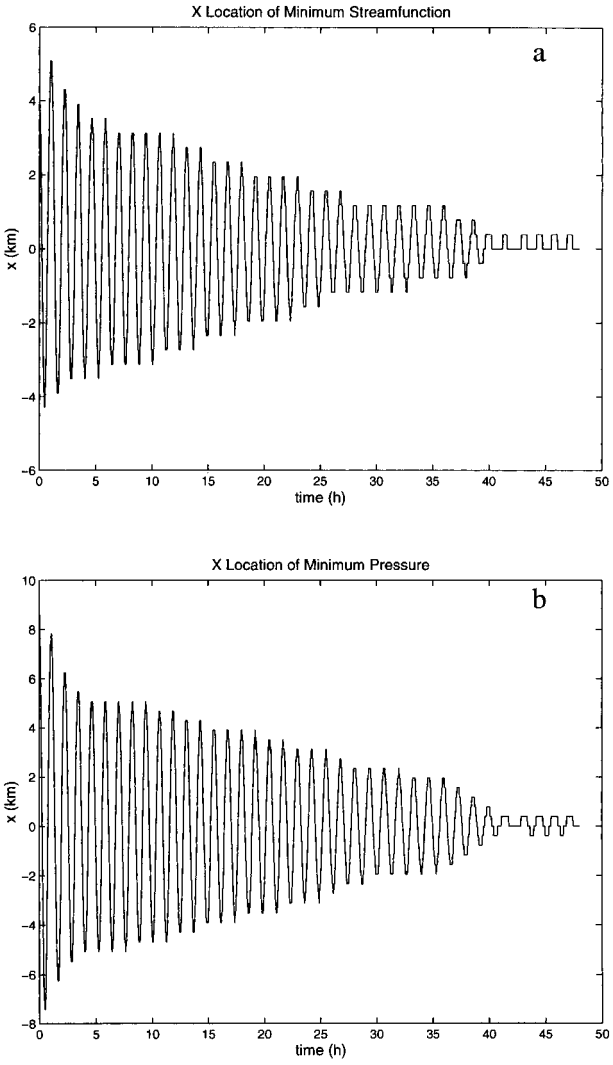

FIG. 6. The x coordinate of the location of the minimum streamfunction (a) and pressure (b) for the high-resolution nonlinear simulation with $\nu = 80$ m^2 s^{-1}.

function and pressure minima slowly migrate back toward the center as the low vorticity core moves away.

Eventually, the low vorticity core reaches the outer edge of the eyewall, where it is sheared apart by the large angular velocity gradients in that part of the vortex. The low vorticity is then quickly redistributed around the outer edge of the eyewall region, while the high vorticity associated with the positive part of the initial wavenumber-one perturbation finds its way to the vortex center. Thus, the azimuthally averaged vorticity profile is redistributed into one that is monotonically decreasing from the center.

The time required for this redistribution to take place is rather sensitive to the value of the viscosity. The vorticity fields at $t = 24$ h, 36 h, and 48 h are shown for each simulation with $\nu = 80$, 40, 20, and 10 m^2 s^{-1}, respectively, in Figs. 7 and 8. At each time, we can see that the redistribution process is further along in the simulations with higher viscosity. It appears that the rate at which the low-vorticity core moves outward through the eyewall region decreases with decreasing viscosity. The slow outward movement of the low-vorticity core is quite similar to the behavior of vortex holes observed by Huang et al. (1995) that were produced by the growth of a wavenumber-two instability in a similar, but exponentially unstable, vortex modeled by an electron plasma. In their experiments, the vortex holes remained coherent for hundreds of vortex circulation times, but also slowly migrated outward from the vortex core until they were destroyed by the strong shear at the outer edge of the vortex. A theoretical basis for understanding the motion of vortex holes in an inviscid fluid has been provided by Schecter and Dubin (1999), who showed that vortex holes tend to move down the vortex gradient of the surrounding flow, while positive vortex anomalies (''clumps'') tend to move up the gradient. In this case, since the background vorticity is increasing outward, the hole should then move inward, or at the very least, remain trapped in the vortex core. Since the vortices do move outward, and their rate of outward motion is clearly dissipation-dependent, it seems that the outward migration is related to dissipative effects. The hole may survive indefinitely in a truly inviscid fluid. Perhaps there exists a steady, nonlinear solution of the Euler equations that emulates the observed wobble, much as the well-known Kirchoff's vortex solution (Lamb 1932, section 159) for an elliptical, piecewise constant vorticity patch emulates the long-lived wavenumber-two asymmetry simulated by Huang et al. (1995), often referred to as the ''tripole.''

Such behavior is probably irrelevant for the inner cores of hurricanes, due to asymmetries in the environment, baroclinic aspects of the vortex, the effects of convection, and turbulent diffusion. Nonetheless we have identified the fully nonlinear behavior of the wavenumber one algebraic instability for two-dimensional, hurricane-like vortices. The instability causes the low vorticity core of the vortex to wobble outwards from the center, resulting in a small-amplitude wobble of the vortex center as defined both by streamfunction and pressure minima. Eventually the instability leads to a complete rearrangement of the inner-core vorticity, such that the vorticity profile is monotonically decreasing from the center and the core of the vortex is nearly in solid-body rotation. Similar rearrangement of inner-core vorticity has in fact been inferred from observational data of hurricanes (Kossin and Eastin 2001).

3. The wavenumber-one instability in a shallow-water fluid

a. The equations of motion and their numerical solution

The equations of motion in cylindrical (r, λ) coordinates for the evolution of a shallow-water fluid on an f plane are,

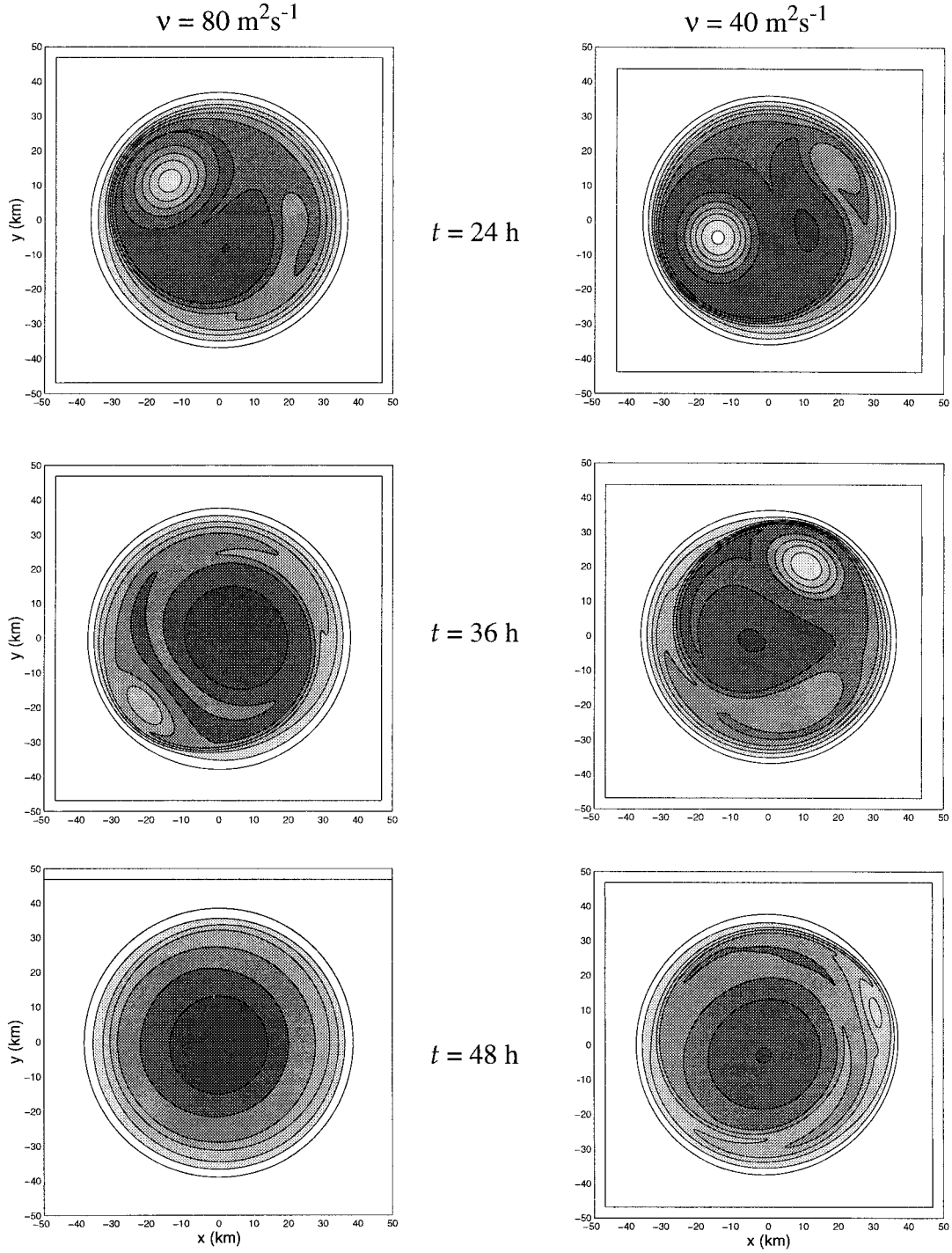

FIG. 7. Snapshots of the vorticity field at 24, 36, and 48 h for nonlinear simulations with $\nu = 40$ and 80 m^2 s^{-1}, as labeled. Units of vorticity: s^{-1}. Contour levels and shading are as in Fig. 4.

$$\frac{Du}{Dt} - \frac{v^2}{r} - fv + g\frac{\partial h}{\partial r} = 0, \tag{3.1}$$

$$\frac{Dv}{Dt} + \frac{uv}{r} + fu + \frac{g}{r}\frac{\partial h}{\partial \lambda} = 0, \quad \text{and} \tag{3.2}$$

$$\frac{Dh}{Dt} + h\left[\frac{1}{r}\frac{\partial}{\partial r}(ru) + \frac{1}{r}\frac{\partial v}{\partial \lambda}\right] = 0, \tag{3.3}$$

where r is the distance from the center axis, λ is the azimuthal angle about the axis, u and v are the radial

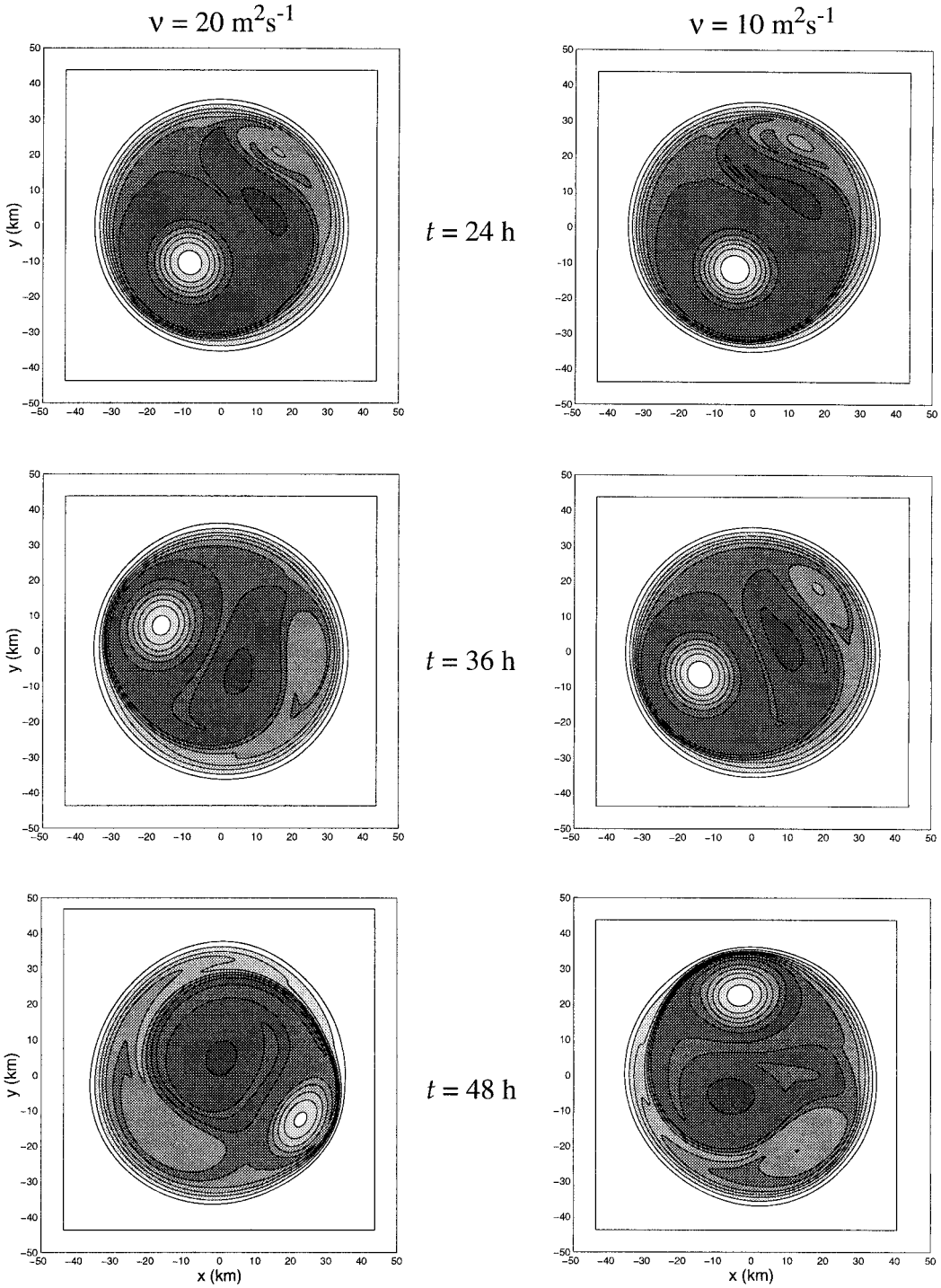

FIG. 8. As in Fig. 7, but for $\nu = 20$ and 10 m^2 s^{-1}.

and azimuthal winds, h is the height of the free surface, g is the gravitational acceleration, f is the Coriolis parameter, and $D/Dt = \partial/\partial t + u(\partial/\partial r) + (v/r)(\partial/\partial\lambda)$ is the material derivative.

We consider the evolution of small perturbations about a basic-state vortex in gradient wind balance,

$$g\frac{\partial \overline{h}}{\partial r} = f\overline{v} + \frac{\overline{v}^2}{r}, \tag{3.4}$$

where $\overline{v} = \overline{v}(r)$ is the basic-state azimuthal wind field, and $\overline{h} = \overline{h}(r)$ is the basic-state height of the free surface. The equations of motion (3.1)–(3.3) are linearized about

the basic state (3.4), and the perturbation u', v', and h' fields are then written in terms of azimuthally varying harmonics for each azimuthal wavenumber n:

$$[u', v', h'] = [u_n(r, t), v_n(r, t), h_n(r, t)]e^{in\lambda}, \quad (3.5)$$

where, rather than assuming exponential time dependencies, we have left the time dependence explicit in the complex functions u_n, v_n, h_n. For each azimuthal wavenumber n, the equations of motion become

$$\frac{\partial u_n}{\partial t} + in\overline{\Omega}u_n - (f + 2\overline{\Omega})v_n + g\frac{\partial h_n}{\partial r} = 0, \quad (3.6)$$

$$\frac{\partial v_n}{\partial t} + in\overline{\Omega}v_n + \left(f + \overline{\Omega} + \frac{\partial \overline{v}}{\partial r}\right)u_n + g\frac{in}{r}h_n = 0, \quad (3.7)$$

and

$$\frac{\partial h_n}{\partial t} + in\overline{\Omega}h_n + \overline{h}\frac{1}{r}\frac{\partial}{\partial r}(ru_n) + \overline{h}\frac{in}{r}v_n + u_n\frac{\partial \overline{h}}{\partial r} = 0, \quad (3.8)$$

where $\overline{\Omega} = \overline{v}/r$ is the basic-state angular velocity.

We solve for the stability and time evolution of the system (3.6)–(3.8) numerically in a manner following Montgomery and Lu (1997) and Flatau and Stevens (1989). A finite domain is prescribed from $r = 0$ to some large outer radius $r = R$. On this domain we define values of h_n to exist at the points $r = j\Delta r$, where $j = 0,1, \ldots N$, and $\Delta r = R/N$. Here u_n and v_n values exist at the ''half'' points $r = (k - 1/2)\Delta r$, with $k = 1, 2, \ldots, N$. Derivatives computed from centered differences between two adjacent grid points on the h grid fall naturally on the uv grid, and similar derivatives on the uv grid fall naturally on the h grid. Where data must be interpolated from one grid to another, as in the last terms of (3.7) and (3.8), a simple average of adjacent points is used. Explicit boundary conditions are needed for the h_n only. At the outer wall, we set $h_n(N) = 0$. At $r = 0$ the natural boundary condition for the perturbation height must be $h_n(0) = 0$, so that singular behavior does not occur as one moves around the azimuth as $r \to 0$. [For $n = 0$ we would use the condition $\partial h_n/\partial r = 0$, but no calculations with symmetric perturbations are presented here.] For most of the calculations presented here, we use a grid spacing $\Delta r = 500$ m and we place the outer boundary at $r = 250$ km. For all calculations we use $f = 5.0 \times 10^{-5}$ s^{-1}, which corresponds to a latitude of 20°N.

Gravity waves are an essential aspect of the dynamics of the shallow water equations. As we will show below, both balanced and unbalanced initial conditions (the meaning of ''balanced'' will be discussed shortly) will produce gravity waves that radiate outward from the vortex core. To prevent substantial gravity-wave reflection from the outer boundary, we use a Rayleigh-damping sponge layer at the outer limits of the domain, which is implemented by adding the terms $-\varepsilon(r)u_n$, $-\varepsilon(r)v_n$, and $-\varepsilon(r)h_n$ to the right-hand sides of (3.6)–(3.8), respectively. The damping function is defined by,

$$\varepsilon(r) = \begin{cases} 0 & r < r_{\text{start}} \\ \varepsilon_{\max} S\left(\dfrac{r_{\text{end}} - r}{r_{\text{end}} - r_{\text{start}}}\right) & r_{\text{start}} \le r \le r_{\text{end}} \\ \varepsilon_{\max} & r > r_{\text{end}}, \end{cases} \quad (3.9)$$

where r_{start} is the beginning of the transition region into the sponge layer, r_{end} is the end of the transition region, $S(x) = 1 - 3x^2 + 2x^3$ is the cubic Hermite polynomial, which has $S'(0) = S'(1) = 0$, $S(0) = 1$, $S(1) = 0$, and $\varepsilon_{\max} = 1/\tau_{\min}$ is the maximum damping rate with time scale $\tau_{\min}$. For all simulations presented here, we use $r_{\text{start}} = 190$ km, $r_{\text{end}} = 240$ km, and $\tau_{\min} = 30$ s.

Through standard techniques, the system of coupled linear equations (3.6)–(3.8), represented in terms of finite differences, can be expressed as a linear dynamical system:

$$\frac{d\mathbf{x}}{dt} = \mathbf{T}_n\mathbf{x}, \quad (3.10)$$

where $\mathbf{T}_n$ is the time evolution operator and the column vector $\mathbf{x}$ contains the values of h_n on the interior of the h grid and u_n and v_n on the uv grid. This representation serves two purposes. First, the stability properties and the eigenfunctions of the system can be determined directly from numerical analysis of the matrix $\mathbf{T}_n$; and second, numerical integration of (3.10) is straightforward with either explicit (such as Runge–Kutta) or implicit (such as Crank–Nicholson) schemes, or even with matrix exponentiation.

b. Potential vorticity, divergence, and balanced flow

Potential vorticity is a useful concept since it is conserved by parcels in the flow. If, in addition, the flow is in quasigeostrophic balance, the height and velocity fields can be uniquely determined from the PV. This result can be generalized to the case of quasi-gradient balance as will be discussed shortly. Indeed, whether or not the inner-core dynamics of intense geophysical vortices obey similar balance principles has been a topic of some research (McWilliams 1985; Raymond 1992; Shaprio and Montgomery 1993; Montgomery and Lu 1997; Möller and Montgomery 2000), and we will show that balanced dynamics also apply to asymmetric perturbations to our shallow-water vortex.

In a shallow water fluid, potential vorticity can be defined as

$$q = \frac{\zeta + f}{h}, \quad (3.11)$$

where ζ is the relative vertical vorticity, f is the Coriolis parameter, and h is the fluid depth (Pedlosky 1987). If we then expand the terms on the rhs of (3.11) into basic state and perturbation parts, and neglect second-order terms, the perturbation PV that naturally appears is

$$q' = \frac{\zeta'}{\overline{h}} - \frac{\overline{q}h'}{\overline{h}}, \tag{3.12}$$

where $\overline{q} = (\overline{\zeta} + f)/\overline{h}$ is the basic-state PV. The vorticity and divergence for asymmetric perturbations are, respectively,

$$\zeta_n = \frac{1}{r}\frac{\partial}{\partial r}(rv_n) - \frac{in}{r}u_n, \quad \text{and} \tag{3.13}$$

$$\delta_n = \frac{1}{r}\frac{\partial}{\partial r}(ru_n) + \frac{in}{r}v_n. \tag{3.14}$$

Using (3.6)–(3.8) and (3.11)–(3.14), one can derive PV and divergence forms of the equations of motion:

$$\frac{\partial q_n}{\partial t} + in\overline{\Omega}q_n + u_n\frac{\partial \overline{q}}{\partial r} = 0, \quad \text{and} \tag{3.15}$$

$$\frac{\partial \delta_n}{\partial t} + in\overline{\Omega}\delta_n + \frac{in}{r}u_n\left(\overline{\eta} + r\frac{\partial \overline{\Omega}}{\partial r}\right) - \frac{1}{r}\frac{\partial}{\partial r}(r\tilde{f}v_n) + g\nabla_n^2 h_n = 0, \tag{3.16}$$

where $\overline{\eta} = f + 1/r\ \partial/\partial r(r\overline{v})$ is the absolute mean vorticity, $\tilde{f} = f + 2\overline{\Omega}$ is the modified Coriolis parameter, and the Laplacian operator for wavenumber n is,

$$\nabla_n^2 h_n = \frac{\partial^2 h_n}{\partial r^2} + \frac{1}{r}\frac{\partial h_n}{\partial r} - \frac{n^2}{r^2}h_n. \tag{3.17}$$

(3.15) and (3.16), along with (3.8), describe an alternative but complete set of equations for the asymmetric perturbations, provided one also solves elliptic equations that find the rotational and divergent parts of the velocity fields from the PV and the divergence, respectively. The system can be further simplified if we assume that the divergence and its material time rate of change ($D_V/Dt = \partial/\partial t + in\overline{\Omega}$) are small compared to the other terms in (3.16), consistent with scaling analysis and theory of quasi-balanced flow, as discussed by McWilliams (1985), Raymond (1992), and Montgomery and Franklin (1998). Then (3.16) becomes simply an elliptic equation for the perturbation height field

$$g\nabla_n^2 h_n = \frac{1}{r}\frac{\partial}{\partial r}(r\tilde{f}v_n) - \frac{in}{r}u_n\left(\overline{\eta} + r\frac{\partial \overline{\Omega}}{\partial r}\right), \tag{3.18}$$

where u_n and v_n are nondivergent velocities obtained from the PV relationship

$$\nabla_n^2\psi_n = \zeta_n = \overline{h}q_n + \overline{q}h_n, \quad \text{and} \tag{3.19}$$

$$u_n = -\frac{in}{r}\psi_n, \qquad v_n = \frac{\partial \psi_n}{\partial r}. \tag{3.20}$$

Note that (3.18), (3.19), and (3.20) are in fact a coupled set of linear equations, so that the exact solution for h_n and the nondivergent velocities cannot be computed immediately from the PV as in quasigeostrophic theory. Rather, to compute the balanced state, we first compute ψ_n from (3.19) using $h_n = 0$ as a first guess. The resulting velocities are put into (3.18) to compute the next guess for h_n, and the process is repeated. In practice we have found convergence is always achieved in just a few iterations.

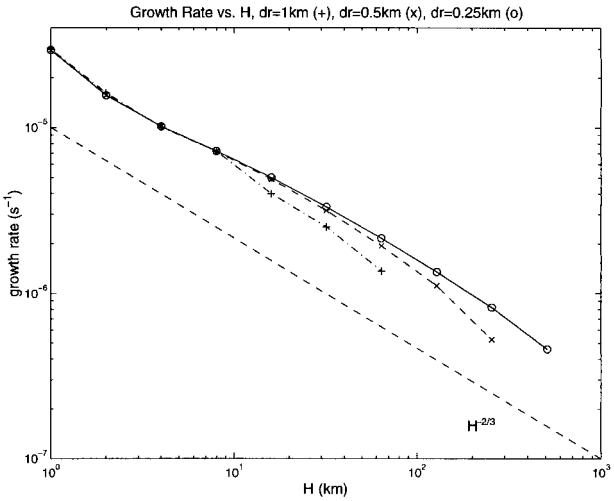

FIG. 9. Growth rate of the most unstable wavenumber-one mode as a function of resting depth H, for calculations with $\Delta r = 1$ km (dash–dot, +), $\Delta r = 0.5$ km (dashed, x), and $\Delta r = 0.25$ km. For $\Delta r = 1$ km, $H > 64$ km, and $\Delta r = 0.5$ km, $H > 256$ km, growth rates were less than 10^{-12}, that is, effectively zero.

c. *The basic-state shallow-water vortex and its stability*

For our shallow-water calculations we use the same basic-state azimuthal velocity field used throughout NM (shown in Fig. 1). We also compute the basic-state height field $\overline{h}(r)$ in gradient wind balance with $\overline{v}(r)$ [cf. (3.4)], given the ''resting'' height H at the outer boundary. Changes in H only result in an equivalent upward or downward displacement of $\overline{h}(r)$.

We first consider the stability of the vortex by computing the eigenvalues and the eigenvectors of the time evolution operator $\mathbf{T}_n$. We find that, unlike the two-dimensional vortex, the shallow-water vortex does in fact support unstable modes; however, the growth rates (real parts of the eigenvalues) of these modes are relatively weak and decrease with increasing resting depth H. This is demonstrated in Fig. 9, which shows the growth rates of the most unstable mode for $n = 1$ for values of $H = 1$ km, 2 km, 4 km. . . , up to 512 km. Results are presented for calculations with $\Delta r = 1000$ m, $\Delta r = 500$ m, and $\Delta r = 250$ m, and are very consistent between these three resolutions for the smaller depths. The growth rates appear to scale with the fluid depth as $H^{-2/3}$, consistent with theory that will be discussed in section 3f. The e-folding times range from 9.5 h for $H = 1$ km to 470.7 h for $H = 512$ km. For the physically relevant depth of $H = 8$ km (approximately

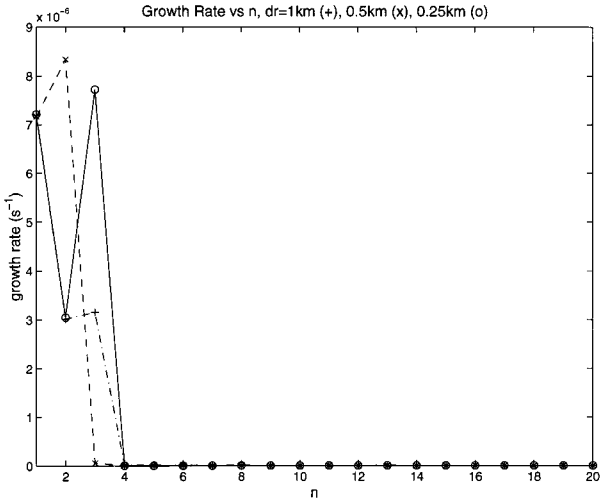

FIG. 10. Stability curves as a function of azimuthal wavenumber n in the NM–shallow water vortex for $H = 8$ km and $\Delta r = 1$ km (dash–dot, +), $\Delta r = 0.5$ km (dashed, x), and $\Delta r = 0.25$ km (solid, ○).

one scale height of the atmosphere), the *e*-folding time of the fastest growing mode is 38.75 h, which is very slow compared to the 1.25-h circulation time of the vortex (or an equivalent hurricane).

Figure 10 shows the growth rates of the most unstable modes as a function of n for calculations with $H = 8$ km, for $\Delta r = 1000$ m, $\Delta r = 500$ m, and $\Delta r = 250$ m. The extremely close correlation in the growth rates of the most unstable mode for $n = 1$ for the three grid spacings indicates that, for wavenumber-one, this mode is well-resolved and robust. Also indicated are unstable modes for $n = 2$ and $n = 3$ whose growth rates are highly dependent on the resolution. These unstable modes are unphysical by-products of the diffusion-free, finite-difference numerical method, in that their vorticity fields contain delta-function-like structures on the scale of the grid spacing, and their structures and eigenvalues are highly sensitive to both the grid spacing and the scheme used to interpolate between the uv and h grids.[3]

The most unstable mode for $n = 1$, $H = 8$ km, and $\Delta r = 500$ m is shown in terms of q_n, h_n, and δ_n in Fig. 11. The structure of the mode (which was virtually identical for different grid spacings) is extremely similar to the growing part of the SR algebraic instability—proportional to the basic-state vorticity gradient, up to RMΩ. However, there appears to be some additional structure to the unstable mode in the vicinity of the RMΩ (the thin, outer PV anomalies), which will be discussed below. The height field is also very similar to the streamfunction field of the algebraic instability,

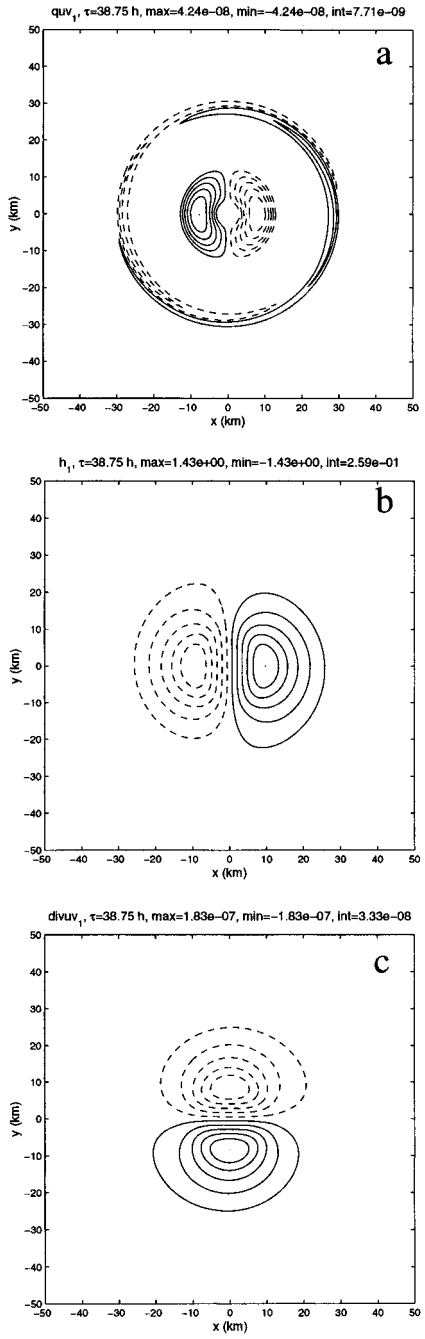

FIG. 11. Structure of the most unstable mode for $H = 8$ km, $\Delta r = 500$ m, in terms of its (a) perturbation PV, in units of shallow-water PV, which are $s^{-1}\ m^{-1}$; (b) perturbation height field (m); and (c) perturbation divergence (s^{-1}). The mode is normalized so that maximum radial velocities are 1 m s^{-1}.

and there is a weak but nonzero divergence field, roughly 3 orders of magnitude smaller than the vorticity (when estimating the vorticity from the PV, recall that $\zeta' \approx \overline{h}q'$). Perhaps most importantly, we find that the height and velocity fields of the unstable mode are virtually identical to the same fields in balance with its PV. The

[3] For example, cubic spline interpolation resulted in different eigenvalues and eigenvectors for $n = 2$ and $n = 3$, but virtually identical results for $n = 1$.

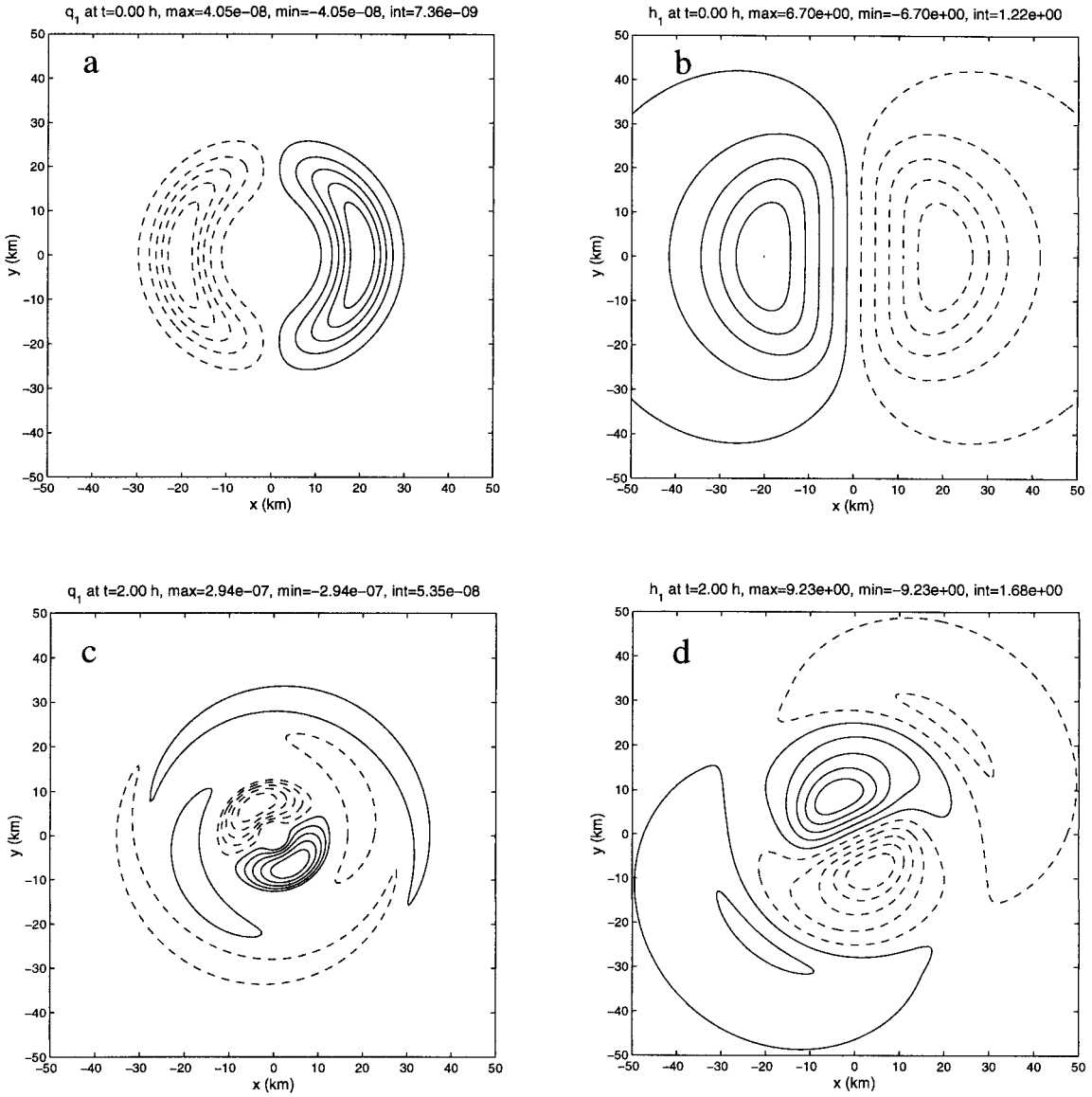

FIG. 12. Evolution of perturbation PV (q') and height (h') fields for the wavenumber-one, balanced perturbation localized at $r = 20$ km: (a) PV, $t = 0$ h; (b) height, $t = 0$ h; (c) PV, $t = 2$ h; and (d) height, $t = 2$ h. (PV units, s^{-1} m^{-1} and height units, m.)

most unstable mode, computed from the linearized primitive equations, is a quasi-balanced flow.

d. Evolution of the wavenumber-one perturbations

We first consider the evolution of a wavenumber-one perturbation whose wind and height fields are in balance with its initial vorticity. The perturbation PV is defined in a manner analogous to the initial perturbation vorticity for the simulations in NM and in section 2 above: a Gaussian perturbation localized in the eyewall, with peak amplitude 10% of the local basic-state flow [i.e., (2.2)–(2.3) with q substituted for ζ]. For these simulations we used a Crank–Nicholson semi-implicit time stepping scheme with $\Delta t = 10$ s. While the time step necessary to accurately resolve the dynamics of gravity waves is just $(\sqrt{gH})/\Delta r = 1.79$ s, we will show later that these waves do not play a role in the evolution of the asymmetric perturbations after the first 15 min. Furthermore, simulations with much shorter time steps gave nearly identical results.

The initial condition and evolution of this perturbation is depicted in terms of its PV and height fields in Figs. 12 and 13. The evolution is nearly identical to that of the equivalent 2D vortex as shown in NM. The 12-h and 24-h PV fields are again nearly identical to the growing part of the SR instability, proportional to $\partial\bar{\zeta}/\partial r$ up to RMΩ. The perturbation kinetic energy versus time is shown in Fig. 14. For the first 24 h, the kinetic energy shows almost exactly the same evolution

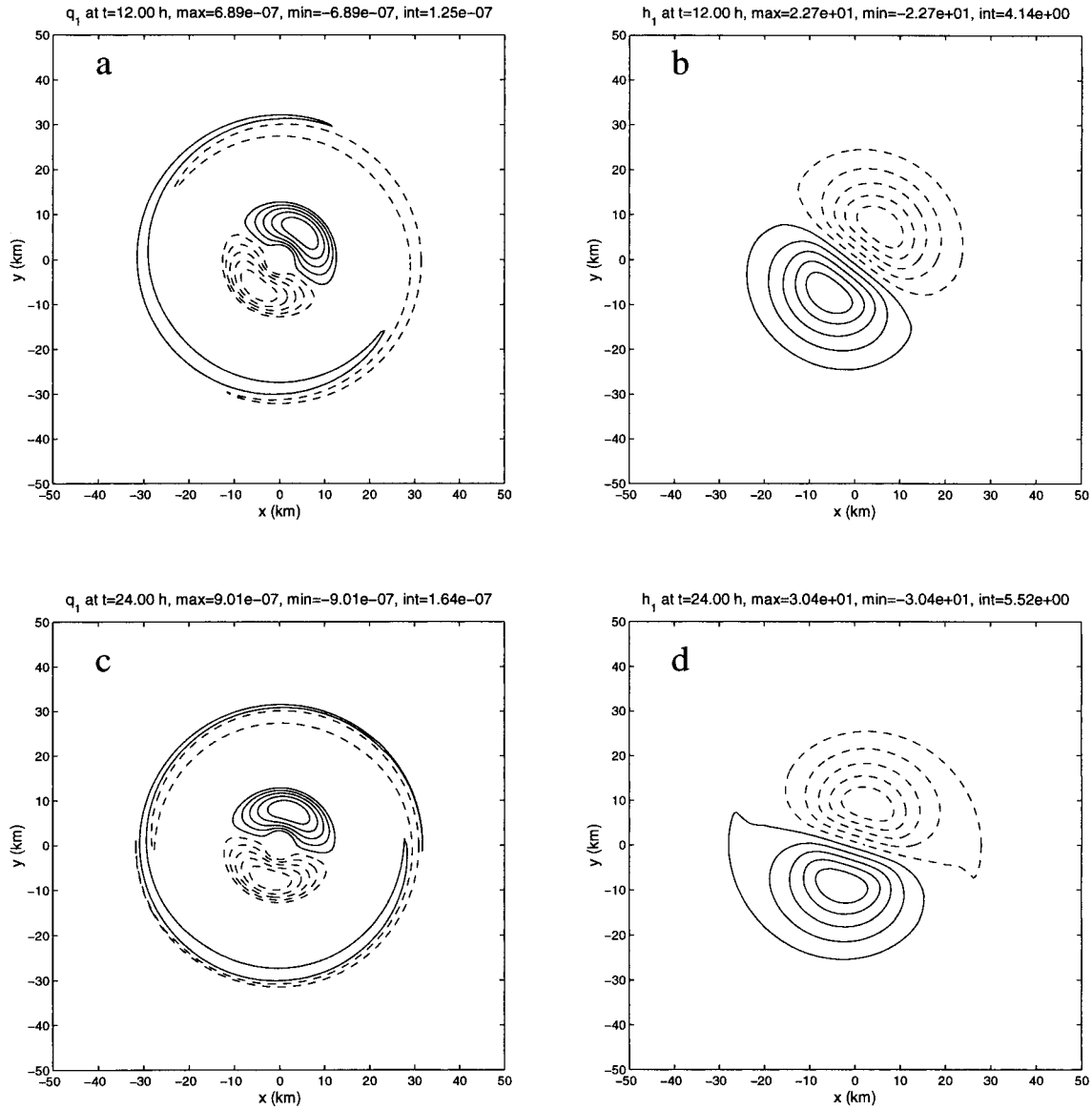

FIG. 13. Evolution of perturbation PV (q') and height (h') fields for the wavenumber one, balanced perturbation localized at $r = 20$ km: (a) PV, $t = 12$ h; (b) height, $t = 12$ h; (c) PV, $t = 24$ h; and (d) height, $t = 24$ h. (PV units, s^{-1} m^{-1} and height units, m.)

as found by NM for 2D dynamics; however, after 24 h the energy growth appears to change from linear to exponential, indicating the rise of the unstable mode. The structure of the unstable mode is close to, but slightly different than the SR instability, and their differences will be shown explicitly. The high-frequency oscillation in the perturbation kinetic energy is caused by an interaction between the rapidly rotating growing instability and the stationary pseudo-mode (see property 2 of the SR instability described in section 1); as these disturbances move in and out of phase with each other the perturbation kinetic energy increases and decreases.

Before further analyzing the differences between the algebraic and exponential instabilities, we first consider the evolution of perturbations from certain special initial conditions. As outlined in section 1, the SR instability will not be excited if the initial perturbation vorticity lies entirely outside of the RMΩ; this was also confirmed by NM with numerical calculations. NM also showed that the initial condition may be adjusted so that there is no excitation of the pseudo-mode, thus eliminating the high-frequency oscillation in the perturbation kinetic energy. This is possible in 2D flow because the excitation of the pseudo-mode is proportional to

$$h(R) = \int_0^R \rho^2 \zeta_1(\rho, 0)\, d\rho. \tag{3.21}$$

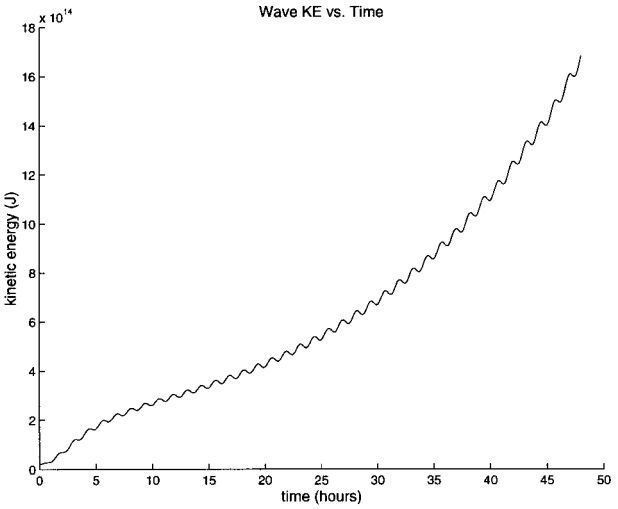

FIG. 14. Perturbation kinetic energy as a function of time for the balanced perturbation localized at $r = 20$ km.

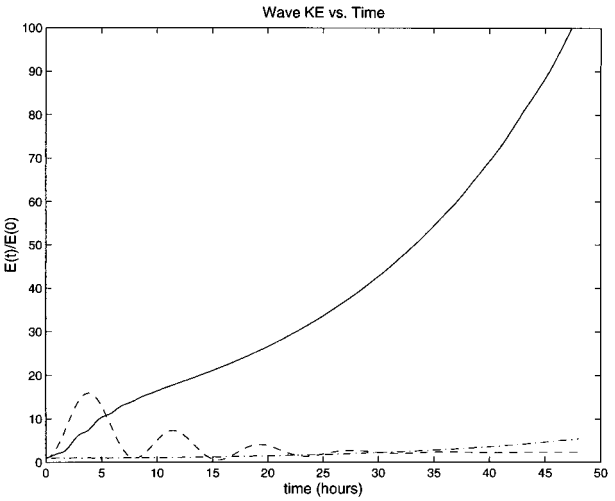

FIG. 15. Perturbation kinetic energies, normalized by initial values, for three special initial conditions: with the pseudo-mode removed (solid), initial PV localized at $r = 80$ km (dashed), and the SR neutral mode (dash–dot).

Thus, the excitation of the pseudo-mode may be eliminated by adding to the original initial condition (2.2) an opposite-signed vorticity anomaly, localized *outside* RMΩ, such that $h(R) = 0$ (see NM section 4c for details). Here, we again replace ζ_1 with q_1 in our calculations.

Results of simulations of the NM–shallow-water vortex with these two special initial conditions are shown in Fig. 15. When the initial perturbation PV lies entirely outside of the RMΩ, no instability is excited, and eventually the perturbation becomes constant in amplitude. The structure of the final state, in fact, is simply the pseudo-mode. Also, with the initial PV modified so that the pseudo-mode is not excited, the high-frequency oscillation in the kinetic energy is eliminated.

The SR solution shows that if the initial vorticity perturbation is exactly proportional to the basic-state vorticity gradient up to RMΩ, that is, $\zeta_1(r, 0) \propto \partial\overline{\zeta}/\partial r$ for $r <$ RMΩ, then the instability will not be excited and long-time growth will not occur. Nolan and Montgomery confirmed this, and further demonstrated numerically that a wavenumber-one perturbation with

$$\zeta_1(r, t) = C\frac{\partial\overline{\zeta}}{\partial r}H(\mathrm{RM}\Omega - r), \qquad (3.22)$$

where here H is the Heaviside step function, and C is some complex constant, is in fact a neutral mode that rotates around the center axis with an angular velocity equal to that of $\overline{\Omega}_{\max}$; that is, $\zeta_1(r, t) = \zeta_1(r, 0)e^{-i\overline{\Omega}_{\max}t}$. This can be shown directly, and the proof is given in the appendix.

Does a similar neutral mode exist in our shallow water vortex? Almost, but not quite. We simulated a perturbation with initial PV:

$$q_1(r, 0) = C\frac{\partial\overline{q}}{\partial r}H(\mathrm{RM}\Omega - r). \qquad (3.23)$$

We then defined the initial perturbation height field with two distinct approaches. The first approach uses the observation that if both q_1 and h_1 are proportional to their respective basic-state gradients for all r, then the time evolution of the perturbations will be zero: this the pseudo-mode for a shallow-water vortex. In this spirit, we define

$$h_1(r, 0) = C\frac{\partial\overline{h}}{\partial r}H(\mathrm{RM}\Omega - r) \qquad (3.24)$$

to represent a *localized* displacement of the inner-core, up to RMΩ. [Note that if (3.23) and (3.24) hold, then so does (3.22).] Alternatively, one can define the initial h_n to be that which holds the initial q_n in balance, as described in section 3b. Remarkably, both of these choices result in virtually identical evolutions of the perturbations and their kinetic energies (KE), which is also shown in Fig. 15 (the energies as a function of time of these two initial conditions are so close that they are indistinguishable in the figure). This is because when we use (3.24), there is a discontinuity in the initial height field, and the solution immediately radiates a pulse of inertia-gravity waves that quickly bring the disturbance into balance; the resulting change in kinetic energy, however, is negligible. For both cases, the kinetic energy remains roughly constant for the first few hours (during which the perturbation rotates without a noticeable change in structure), but then begins to increase exponentially (albeit slowly, due to the slow growth rate of the unstable mode). By 48 h the perturbation KE has increased by a factor of only 5.44. At this time, the structure of the disturbance is quite similar to the most unstable mode. We note that *linear* growth in energy does not seem to occur. Thus it appears that using the shallow water equivalent to the SR neutral mode inhibits

the algebraic instability, but nonetheless excites the most unstable mode.

e. Evolution from unbalanced initial conditions

Just as we can generate initial conditions that are nearly balanced, we can also generate initial conditions that are almost completely ''unbalanced.'' This is done by first choosing an arbitrary height perturbation, then computing an associated vorticity field

$$\zeta_n = \frac{\overline{q}}{\overline{h}} h_n, \tag{3.25}$$

such that $q_n = 0$ everywhere [cf. (3.12)], and then computing the initial velocity fields from (3.19) and (3.20). We performed two simulations, one with a height perturbation that is a Gaussian-localized at $r = 20$ km and a maximum amplitude of 50 m, congruent to (2.2), and a similar perturbation localized at $r = 80$ km. For these simulations, we used a much shorter time step, $\Delta t = 2$ s, so that the phase speeds of the resulting gravity waves would be accurately captured. The perturbation kinetic energies as a function of time for these two simulations are shown in Fig. 16a. The ''spikes'' in the kinetic energy just after $t = 0$ are associated with the rapid appearance, outward propagation, and dissipation of gravity waves. While the freely propagating inertia-gravity waves will not generate PV and/or balanced flow on a quiescent f plane, such is not the case when a nontrivial basic state is present (Montgomery and Lu 1997). By interacting with the basic state, each of these solutions projects a small amount of its energy onto the balanced, ''slow manifold,'' such that for the inner perturbation, the wavenumber-one instability is marginally excited, and for the outer perturbation, the final state is just the pseudo-mode as it was for the similar balanced perturbation above (as shown in Fig. 15). A close-up of the early kinetic energy evolution is shown in Fig. 16b. Once the initial gravity wave packet is developed, the waves propagate outwards with nearly constant kinetic energy, until they are dissipated in the damping region beyond $r = 190$ km [cf. (3.9)]. The outward propagation of these waves is depicted in Fig. 17, which shows the complex magnitude of h_n and δ_n at $t = 0$, 30 s, 4 min, and 10 min. Observe that the outer edge of the h_n wave packet is at $r = 100$ km at $t = 240$ s, and at $r = 200$ km at $t = 600$ s. From these two points we can estimate the simulated gravity wave speed to be 277.8 m s^{-1}, less than 1% in error from the theoretical gravity wave speed $(\sqrt{gH})^{1/2} = 280.1$ m s^{-1}. After the waves spread into the damping region, only balanced flow is left behind.

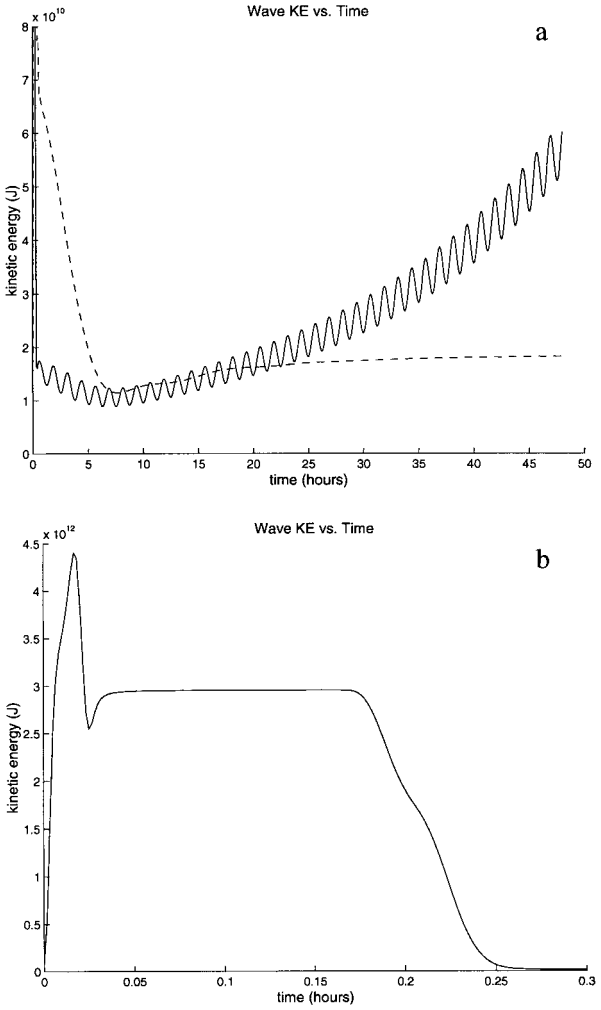

FIG. 16. Perturbation kinetic energies as a function of time from unbalanced initial conditions: (a) evolution out to 48 h, for the perturbations localized at $r = 20$ km (solid) and at $r = 80$ km (dashed), and (b) the evolution for the first hour for the perturbation localized at $r = 20$ km. Note the very different scales along the vertical axis for the two plots, so that the long-time behavior can be analyzed in (a) and the short-time behavior can be analyzed in (b).

f. Mechanisms for algebraic and exponential instability

Both algebraic and exponential instability mechanisms appear to be present in the NM–shallow-water vortex. Exponential instability for $n = 1$ perturbations in vortices with low-vorticity cores was first observed in plasma physics experiments (Driscoll 1990), despite the fact that linear theory predicts there can be no exponentially unstable modes in a two-dimensional, inviscid vortex for wavenumber-one (Reznik and Dewar 1994).[4] The SR solution showed that secular growth can occur, but could not account for the observed exponential growth. Efforts to understand this contradiction between theory and experiments have since followed.

[4] It should be noted that wavenumber-one instabilities were also found to exist in the presence of substantial viscosity by Nolan and Farrell (1999a). Most statements on the existence of exponential instabilities rely on analyses of the inviscid equations, and may not be valid in the presence of viscous dissipation.

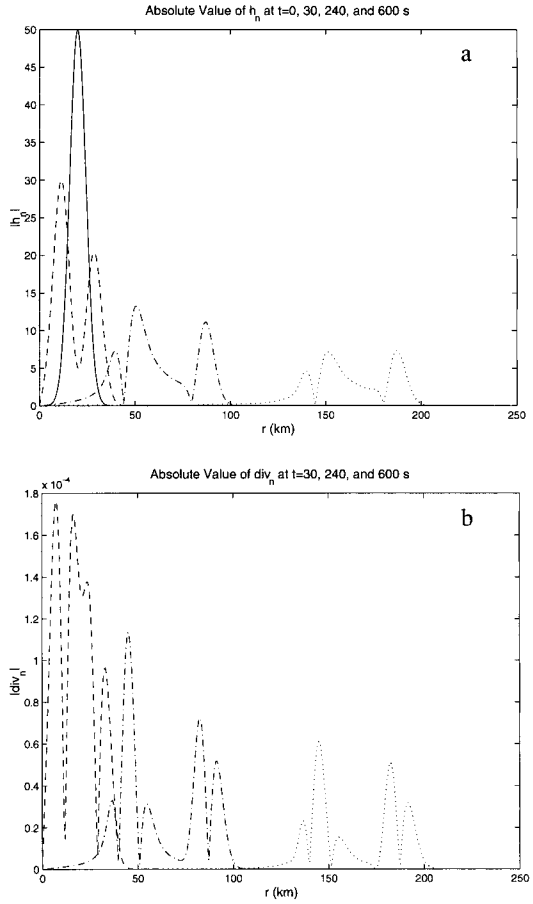

FIG. 17. Evolution of the perturbation height and divergence fields for the unbalanced perturbation localized at $r = 20$ km: (a) complex magnitude of h_n at $t = 0$ (solid), 30 s (dashed), 4 min (dash–dot), and 10 min (dotted); and (b) complex magnitude of δ_n at $t = 30$ s (dashed), 4 min (dash–dot), and 10 min (dotted; values at $t = 0$ are negligible). Height units in meters and divergence units in s^{-1}.

There are three important distinctions between the dynamics of two-dimensional and shallow-water vortices: the presence of freely propagating inertia-gravity waves, the variation of the basic-state height, and the finite value of the Rossby radius of deformation. Inertia-gravity waves clearly do not play a role in the dynamics of either algebraic or exponential growth here, because we have found that within the first few hours of all the simulations the flow evolution occurs via quasi-balanced flow. That the variation of the basic-state height plays a role in the exponential instability has recently been demonstrated by Finn et al. (1999a,b). They found that the ends of the confinement region in the electron plasma experiments are not perfectly flat, but have a small variation with radius from the center of the apparatus. As a result, the vertically averaged electron density, which is equivalent to the two-dimensional vertical vorticity, is not conserved by the flow, but instead the potential density nL is conserved, where n is the electron density and $L = L(r)$ is the length of the confinement region. This obviously bears resemblance to the conservation of potential vorticity $(\zeta + f)/h$. Finn et al. (1999a,b) have shown that wavenumber-one is destabilized for hollow (low-vorticity core) vortices when $L(r)$ decreases with radius, which is equivalent to $\overline{h}(r)$ increasing with radius, as is the case for a balanced, shallow-water cyclonic vortex. This destabilization occurs even when the perturbations to $L(r)$ are neglected; in most of their calculations, Finn et al. (1999a,b) consider the ends of the confinement region to be fixed, much like the motion of a shallow-water fluid between two rigid lids of varying height.

How does the variation of $\overline{h}(r)$ cause the appearance of an exponentially unstable mode for $n = 1$? Consider the SR neutral mode (3.22), which rotates at the frequency $\overline{\Omega}_{\max}$. This frequency is faster than any other perturbation can rotate (in the quasi-balanced regime), and as a result, the SR neutral mode cannot couple with any other perturbation. However, the radial gradient of $\overline{h}(r)$ modifies the PV gradient in such a way as to slow down the mode. To understand azimuthal propagation of asymmetric perturbations on a shallow-water vortex, we turn to asymmetric balance (AB) theory as developed by Shapiro and Montgomery (1993) and Montgomery and Kallenbach (1997). It is well known that in the core of intense vortices such as hurricanes, the Rossby number is large and quasi-geostrophic theory is not valid. However, the effect of rotation on linearized, asymmetric perturbations is not merely f but rather is described by the modified Coriolis parameter $\tilde{f} = f + 2\overline{\Omega}$ and the absolute vorticity $\eta = f + \overline{\zeta}$, [cf. (3.6)–(3.7)] both of which will be substantially larger than f (inside the RMΩ) due to the rapid rotation of the vortex itself. As a result, such perturbations can be described using a localized balance approximation, which is similar to the balance described in section 3b, but which may be extended through a series of approximations so that the motions may be described in terms of a single geopotential $\phi'(r, \lambda, z, t)$ (in the case of a continuous, stratified fluid), much like in quasi-geostrophic theory. Using the AB formulation, Montgomery and Kallenbach (1997) derived a local dispersion relation for the propagation of vortex-Rossby waves in a shallow-water vortex. In particular, consider some *localized* PV perturbation with azimuthal wavenumber n and *radial* wavenumber k. The resulting phase velocity in the azimuthal direction is

$$C_{p\lambda} = R_0\overline{\Omega}_0 + \frac{\tilde{f}_0}{\overline{q}_0}\frac{(\partial\overline{q}_0/\partial r)}{\{k^2 + n^2/R^2) + \gamma_0^2\}}, \quad (3.26)$$

where the zero subscripts refer to local values at some $r = R_0$, and

$$\gamma_0^2 = \frac{\overline{\eta}_0\tilde{f}_0}{g\overline{h}_0} \quad (3.27)$$

is the square of the inverse of the *local* Rossby radius.

Both the SR–neutral mode and the shallow-water un-

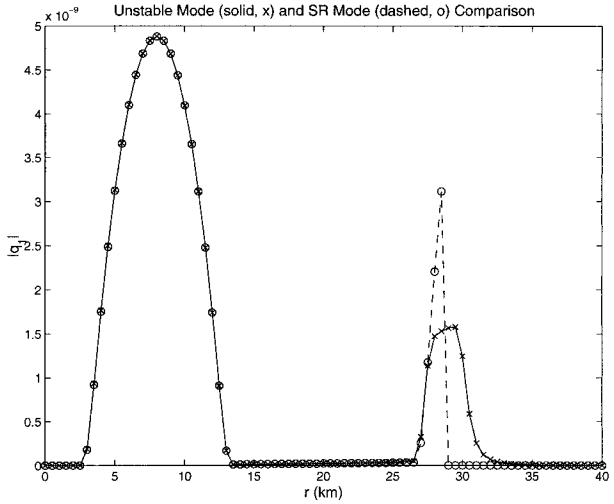

FIG. 18. Structure of the PV of the most unstable mode for $H = 8$ km, $\Delta r = 0.5$ km (solid, with x's), and an amplitude-matched PV equivalent SR neutral mode (dashed, with o's). PV units in $s^{-1}\ m^{-1}$.

stable mode have perturbation vorticity in two localized regions—an inner anomaly associated with the region of positive basic-state vorticity gradient, and an outer region associated with negative basic-state vorticity gradient and $\overline{\Omega}_{\max}$ (cf. Figs. 13a,c). In 2D flow, the inner vorticity anomaly can rotate at the speed of $\overline{\Omega}_{\max}$ because it is in a region of positive PV gradient; that is, it propagates faster than the local mean flow [cf. (3.25)]. Nolan and Montgomery found that the speed of the outer disturbances, which would by themselves propagate slower than $\overline{\Omega}_{\max}$, are in fact increased due to local vorticity production caused by the inner anomalies interacting with the basic-state vorticity gradient. The outer anomalies retard the speed of the inner anomalies, but the effect is minimal due to their small scale.

Note, however, that in the shallow water case this rate of propagation is diminished because

$$\frac{\partial \overline{q}}{\partial r} = \frac{1}{\overline{h}}\frac{\partial \overline{\zeta}}{\partial r} - \frac{\overline{q}}{\overline{h}}\frac{\partial \overline{h}}{\partial r} < \frac{1}{\overline{h}}\frac{\partial \overline{\zeta}}{\partial r}, \tag{3.28}$$

since $\overline{h}$ is increasing monotonically from the center and $\overline{q}$ is positive everywhere. The retardation of the motion of the shallow-water perturbation equivalent to the SR–neutral mode [defined by (3.23)], allows it to couple with other disturbances in the vicinity of $\overline{\Omega}_{\max}$, and together they form an unstable mode. In fact, the angular velocity of the most unstable mode is $1.462 \times 10^{-3}\ s^{-1}$, just slightly less than the maximum angular velocity which is $1.470 \times 10^{-3}\ s^{-1}$. Figure 18 shows a comparison of the complex magnitude of q_n of the unstable mode and a nearly neutral perturbation (3.23) with phase and amplitude chosen to match the most unstable mode as closely as possible. If one subtracts this nearly neutral mode (in terms of its q_n and its associated balanced fields) from the unstable mode, we can see in Fig. 19 the structure of the difference between them, which consists of sheared disturbances in the vicinity of $\overline{\Omega}_{\max}$. In the 2D case, NM showed that the velocity fields induced by such disturbances decay in amplitude with time as $t^{-1/2}$, allowing for the slow but secular growth of the SR–neutral mode.[5] In the shallow-water case, the nearly neutral mode and these disturbances are phase locked and amplifying each other, resulting in exponential instability.

In fact, Finn et al. (1999a,b) showed that, in the fixed depth (no free-surface) approximation, the inner-core mode is slowed by an amount that scales as $\kappa^{2/3}$, where

$$\kappa \sim \frac{L''(r)}{L(0)} \tag{3.29}$$

is a measure of the curvature of the surface normalized by the length of the plasma chamber. The exponential growth, which depends on this slowing of the mode, was also shown to scale as $\kappa^{2/3}$. As shown in Fig. 9, the wavenumber-one growth rates approximately scale with the resting depth as $H^{-2/3}$, consistent with these findings.

The propagation speed is further diminished by the γ_0^2 term in the denominator, which is not present in the purely 2D case [see Montgomery and Kallenbach (1997) or NM]. This term may modify the growth rates as the resting depth H is decreased, although we have not determined the explicit relationship. As the free-boundary effects decrease the angular velocity of the nearly neutral SR mode, the mode can ''interact'' more efficiently with the basic-state flow, allowing for an even faster exponential growth. A similar effect was also observed when free-boundary effects on the containment length $L(r, \lambda, t)$ were considered in the electron plasma experiments of Finn et al. (1999a,b).

4. The wavenumber-one instability in a three-dimensional hurricane-like vortex

We have shown that an instability similar to the SR algebraic instability also appears in a shallow-water vortex with a low-vorticity core. The natural next step is to ask whether a similar instability occurs in a three-dimensional vortex with wind and temperature fields that are representative of actual hurricanes. To answer this question, we have performed fully three-dimensional simulations of such a vortex in a high-resolution mesoscale model.

a. The model

The numerical model used for this simulation is version 3b of the Regional Atmospheric Modeling System (RAMS), developed at Colorado State University (Pielke et al. 1992). The following features of the model were implemented:

[5] The cumulative effect of $t^{-1/2}$ forcing is $\int t^{-1/2}\, dt = 2t^{1/2} + C$.

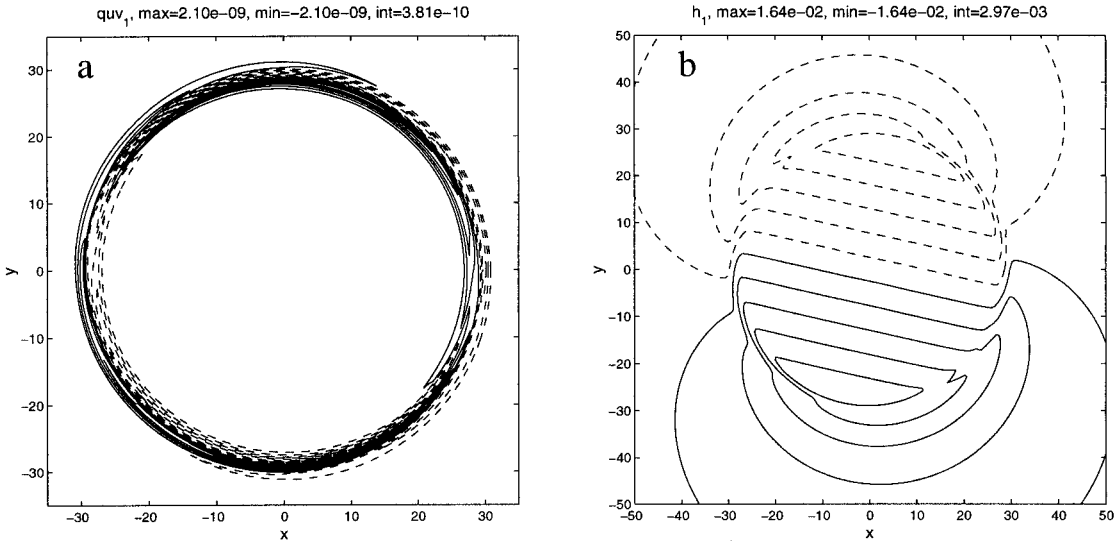

FIG. 19. Spatial structure of the residual PV and balanced height fields computed from the difference between the most unstable mode PV amplitude and phase-matched shallow-water perturbation equivalent to the SR neutral mode: (a) perturbation PV difference, in s^{-1} m^{-1}; and (b) perturbation height difference in m.

- The fluid motions are nonhydrostatic and compressible (Tripoli and Cotton 1982).
- A hybrid time step scheme, where momentum is advanced using a leapfrog scheme and scalars are advanced using a forward scheme. Both use second-order advection.
- Vertical and horizontal turbulence are parameterized using a Smagorinsky (1963) deformation-based eddy viscosity with Richardson number stability modifications (Lilly 1962).
- Prognostic variables are the three components of momentum u, v, and w, the perturbation Exner function π, and potential temperature θ.
- The model uses an Arakawa C fully staggered grid.
- Perturbation Exner function tendencies used to update the momentum variables are computed using a time split scheme, similar to Klemp and Wilhelmson (1978).
- The Klemp–Wilhelmson radiation condition is used on the lateral boundaries, in which the normal velocity component specified at the lateral boundary is effectively advected from the interior.
- The top of the domain has a solid-wall boundary with a 3-km-deep friction (Rayleigh damping) layer below.
- The lower boundary condition is free-slip.

A horizontal grid spacing of 1 km is used within a domain covering 350 × 350 km. The domain extends to a height of 23.0 km with vertical grid spacings of 1000 m. The initial sounding is the Jordan (1958) mean hurricane season sounding. The simulation ran for 12 h with a time step of 10 s. The Coriolis parameter has the uniform value $f = 5.0 \times 10^{-5}$, which corresponds to 20°N.

Furthermore, the model was utilized without a number of features typical of mesoscale simulations: no moisture is included and there are no moist or radiative processes involved. Thus the simulation is a highly idealized representation of the evolution of a dry, balanced, hurricane-like vortex.

b. The basic-state vortex

We wish to construct a basic state vortex that is similar to that of an actual hurricane, and shares some of the same stability properties as the NM vortex used above. We begin by extending the NM velocity profile into the vertical, by using analytic functions to cause an appropriate decay of the wind field with height; that is,

$$\overline{V}(r, z) = \overline{v}(r) \exp\left[-\left(\frac{1.7z}{z_{\text{top}}}\right)^{2.0}\right] \times \left\{1.0 - \exp\left[-\left(\frac{r}{\alpha + 4z}\right)^{2.7}\right]\right\}, \quad (4.1)$$

where $\overline{v}(r)$ is the NM velocity profile, r and z are the distances from the center axis and the altitude, respectively, and $z_{\text{top}} = 16$ km is approximately the upper limit of the wind field. The first multiplicative factor on the rhs of (4.1) is a decay function, which causes the velocity field to decay suitably with height, as is observed in hurricanes (for examples of height–radius profiles of observed hurricane wind fields, see e.g., Marks 1992; Dodge et al. 1999). The second multiplicative factor has an r dependence that causes the inner core wind field (i.e., the eyewall) to slope outward with height, as is also observed. The parameter α serves only to prevent the last bracketed term from being undefined at $z = 0$; we use $\alpha = 1.0$ m. The basic-state wind field is shown in Fig. 20a.

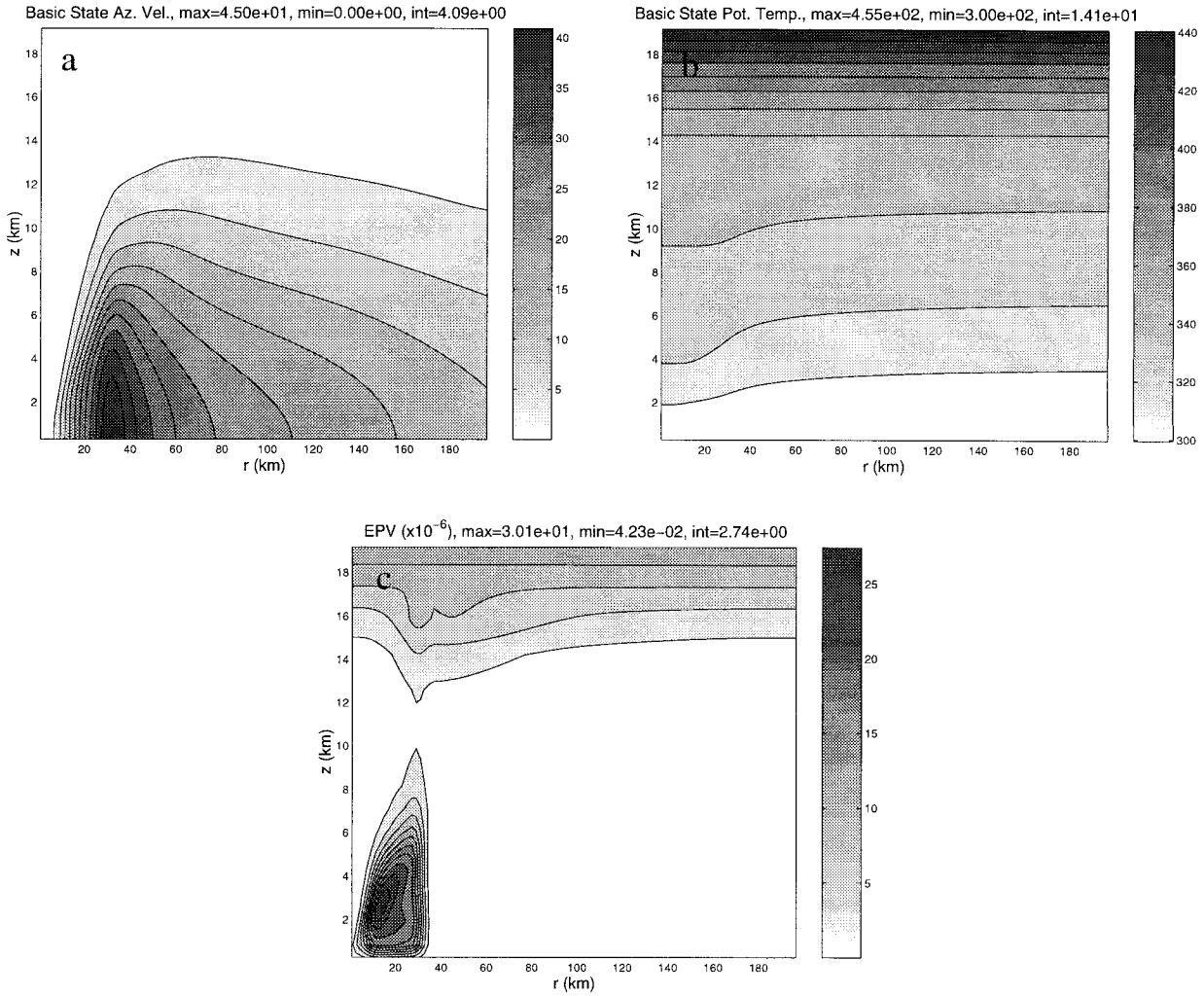

FIG. 20. Basic-state (a) azimuthal velocity in m s^{-1}, (b) potential temperature, and (c) Ertel's PV for the balanced, hurricane-like vortex.

Next, we must find pressure temperature fields that hold this vortex in hydrostatic,

$$\frac{\partial \overline{p}(r, z)}{\partial z} = -\overline{\rho}(r, z)g, \tag{4.2}$$

and gradient wind,

$$\frac{\partial \overline{p}(r, z)}{\partial r} = \overline{\rho}(r, z)\left\{ f\overline{V}(r, z) + \frac{\overline{V}(r, z)^2}{r} \right\}, \tag{4.3}$$

balance. This is achieved with the following iterative procedure. First, we initialize the axisymmetric pressure and temperature fields using the Jordan (1958) observed mean hurricane season soundings from the West Indies. Next, we compute the pressure field by integrating (4.3) inward from the outer boundary, while holding the temperature field at its current value. Then, we correct the temperature (and density) fields by enforcing the hydrostatic condition (4.2) everywhere, while holding the pressure at its current value. This process is repeated (typically 5–7 times) until the fields converge to a solution. These computations are performed on a two-dimensional, evenly spaced grid with 0.5-km resolution in both the r and z directions, with a maximum radius of 200 km and a maximum height of 22 km. The final data is then interpolated onto the RAMS three-dimensional Cartesian grid to provide the basic-state vortex. The basic-state potential temperature and Ertel's potential vorticity fields are shown in Figs. 20b and 20c. Note the familiar warm core and the ''hollow tower'' of PV. Although the vortex has been constructed without a boundary layer, there is a local maximum in the PV above the surface at $z = 2.5$ km; this is quite similar to the PV field produced in a recent high-resolution simulation of an intensifying hurricane modeled after Hurricane Andrew (1992; Chen and Yau 2001).

c. Initial conditions and results

For the initial conditions, we also add to this axisymmetric wind field a wavenumber-one perturbation

similar to those used above. We first obtain the two-dimensional wind field $u'(r, \lambda)$, $v'(r, \lambda)$ generated by the same wavenumber-one vorticity perturbation used in NM. We then extend the perturbation wind field into the vertical with

$$[u'(r, \lambda, z), v'(r, \lambda, z)] = [u'(r, \lambda), v'(r, \lambda)] \exp\left[-\left(\frac{1.8z}{z_{\text{mode}}}\right)^{3.0}\right], \quad (4.4)$$

where we have used a similar exponential decay factor with height as in (4.1), and $z_{\text{mode}} = 14$ km. While the pressure and temperature fields are not in balance with this perturbation, its small amplitude prevents the resulting adjustment process from affecting the results significantly.

The evolution of this perturbed hurricane-like vortex was simulated for 12 h. The initial conditions and early evolution of the PV fields at 30-min intervals from $t = 0$ h to $t = 2.5$ h are shown in Figs. 21 and 22, both at $z = 0.5$ km and $z = 4.5$ km. At $z = 0.5$ km, we see the familiar growing wobble of the low-vorticity core. At $z = 4.5$ km, the amplitude of the vorticity perturbation and the resulting wobble are considerably less, as is the speed at which they rotate around the center, since the azimuthal winds are substantially slower at this altitude (about 35 m s^{-1}). Unlike the two-dimensional simulations, the growing disturbance begins to develop some rather complex structure within the first 6–12 h, as is shown in Fig. 23. This is due to the different rotation speeds with height of the vorticity perturbations, leading to stronger vertical gradients in velocity and vorticity, and ultimately to instabilities with complex structures in the vertical as well as horizontal directions. Even at this stage, however, the maximum vertical velocities are 25 cm s^{-1} or less (not shown), such that the dynamics remain quasi-balanced. The effect of these secondary instabilities is to cause an even more rapid rearrangement of the inner-core vorticity. Note how at $t = 12$ h, some of the highest vorticity at $z = 0.5$ km has arrived at the vortex center, similar to the results for purely two-dimensional flow shown in Figs. 7 and 8. At $z = 4.5$ km, the instability is not nearly as robust and the low-vorticity core remains while the wavenumber-one perturbations have been axisymmetrized in the near field.

The wobble of the low-level center, as indicated by the location of the minimum pressure, can also be seen in the mesoscale simulation. This is demonstrated in Fig. 24, where we show the lowest contourable pressure level at the lowest model level ($z = 500$ m) at 30-min intervals in the simulation. These pressure contours give a clearer indication of the location of the minimum pressure rather than simply indicating the gridpoint locations of the lowest pressure value, because such locations can only fall on the 1-km-spaced grid points (consider what the last 12 h of data in Fig. 6 would be like if the grid spacing were three times larger in those simulations). As we saw with the high-resolution, two-dimensional simulations, the amplitude of the wobble only increases for the first few hours, then steadily declines as the instability transitions to nonlinear dynamics and inner-core mixing. Another imporant point is that the minimum pressure steadily declines as the inner-core vorticity rearrangement proceeds; this is exactly the process Emanuel (1997) requires for a hurricane to reach its MPI.

5. Conclusions

We have investigated the instability of wavenumber-one perturbations to hurricane-like vortices with low-vorticity cores. We find that the instability is a robust feature of such vortices.

In purely two-dimensional flow, the remarkable SR solution predicts that the instability will grow in time as $t^{1/2}$, and was confirmed and studied in some detail by NM. Here, high-resolution simulations of the instability in purely two-dimensional flow show that the instability leads to a redistribution of the inner-core vorticity, with the highest vorticity accumulating at the center of the vortex within 24 h. Given sufficient time, the low-vorticity core is eventually ejected from the inner core of the vortex and symmetrized in the surrounding environment. While we found that the timescale for this ejection process depended strongly on the viscosity, such behavior is likely only relevant for related plasma physics experiments and other effectively two-dimensional flows.

The shallow-water equations allow for the important additional phenomena of vortex stretching, gravity waves, and gradient adjustment. In such an environment, the wavenumber-one instability becomes an exponential instability, with a structure nearly identical to that of the algebraic instability, representing a displacement of the low-vorticity core relative to the surrounding flow. The transition of the algebraic instability to the exponential instability is caused by a slowing of the propagation of vortex-Rossby waves, caused both by the variation of the basic-state height, and also finite Rossby radius effects. These effects allow the SR–neutral mode to couple more effectively with other perturbations and form an unstable mode. For fluid depths relevant to hurricane-like vortices, the growth rates are fairly slow such that the exponential growth is comparable to the algebraic growth on the relevant time scales of 6 to 24 h.

Finally, we have shown that a very similar instability will appear when a three-dimensional, balanced vortex with a hurricane-like wind field is initialized with a wavenumber-one perturbation. For the first few hours, the evolution of the low-level PV is nearly identical to what has been seen in 2D flow and in the shallow-water equations. However, within 12 h the differential rotation of the vortex with height leads to three-dimensional (though still quasi-balanced) instabilities and then to a

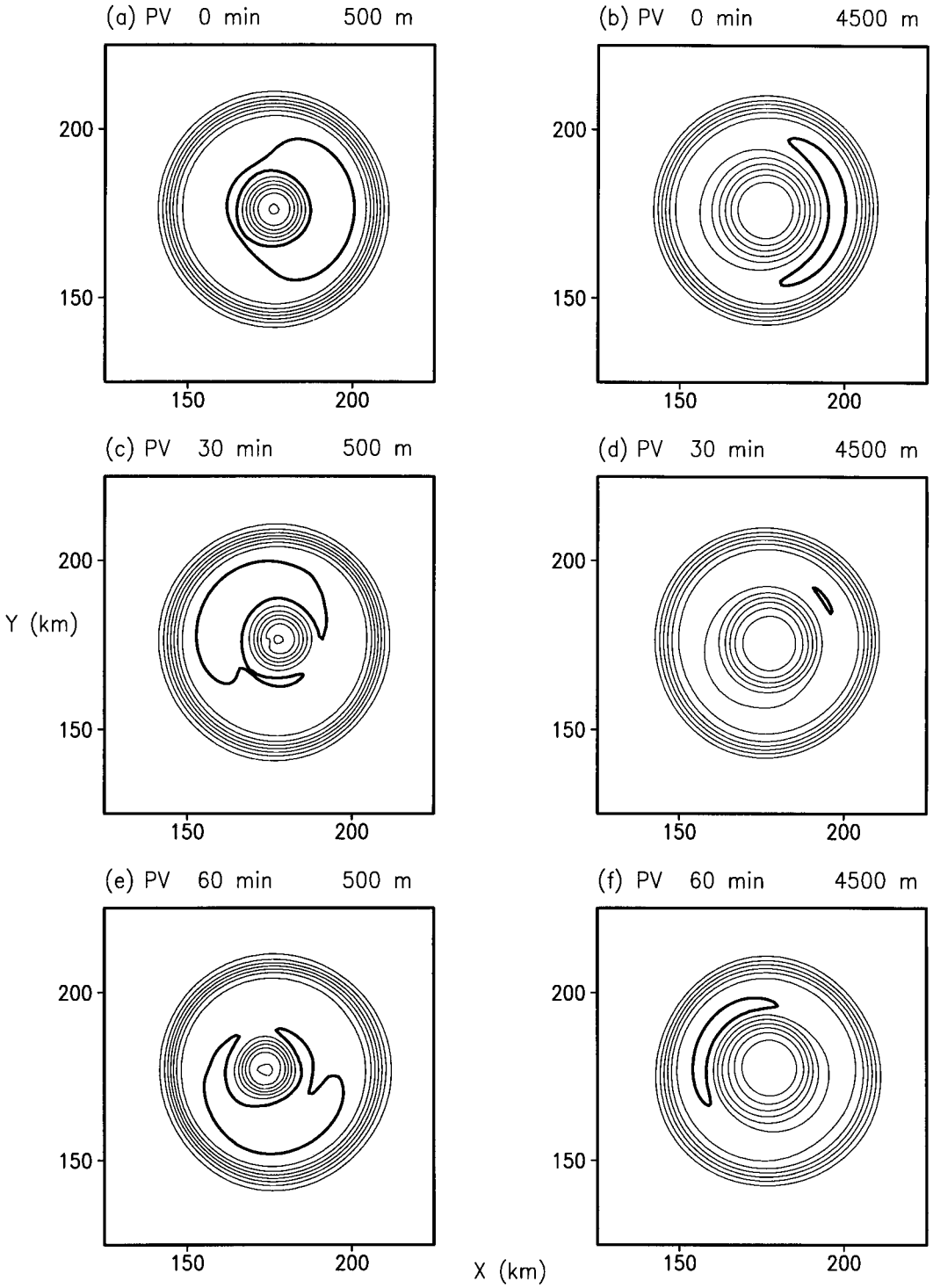

FIG. 21. Early evolution of the Ertel's PV in the mesoscale model simulation every 30 min, at $z = 0.5$ km and $z = 4.5$ km, as labeled. Contours at $z = 500$ m are at 1.25, 2.5, 3.75, 5.0, 6.25, 7.5, 8.75, and 10.0 PV units (equal to 10^{-6} m^2 K s^{-1} kg^{-1}). Contours at $z = 4500$ m are 3, 6, 9, 12, 15, 18, and 21 PV units. The highest contour levels in each case are thick, so that local maxima can be identified.

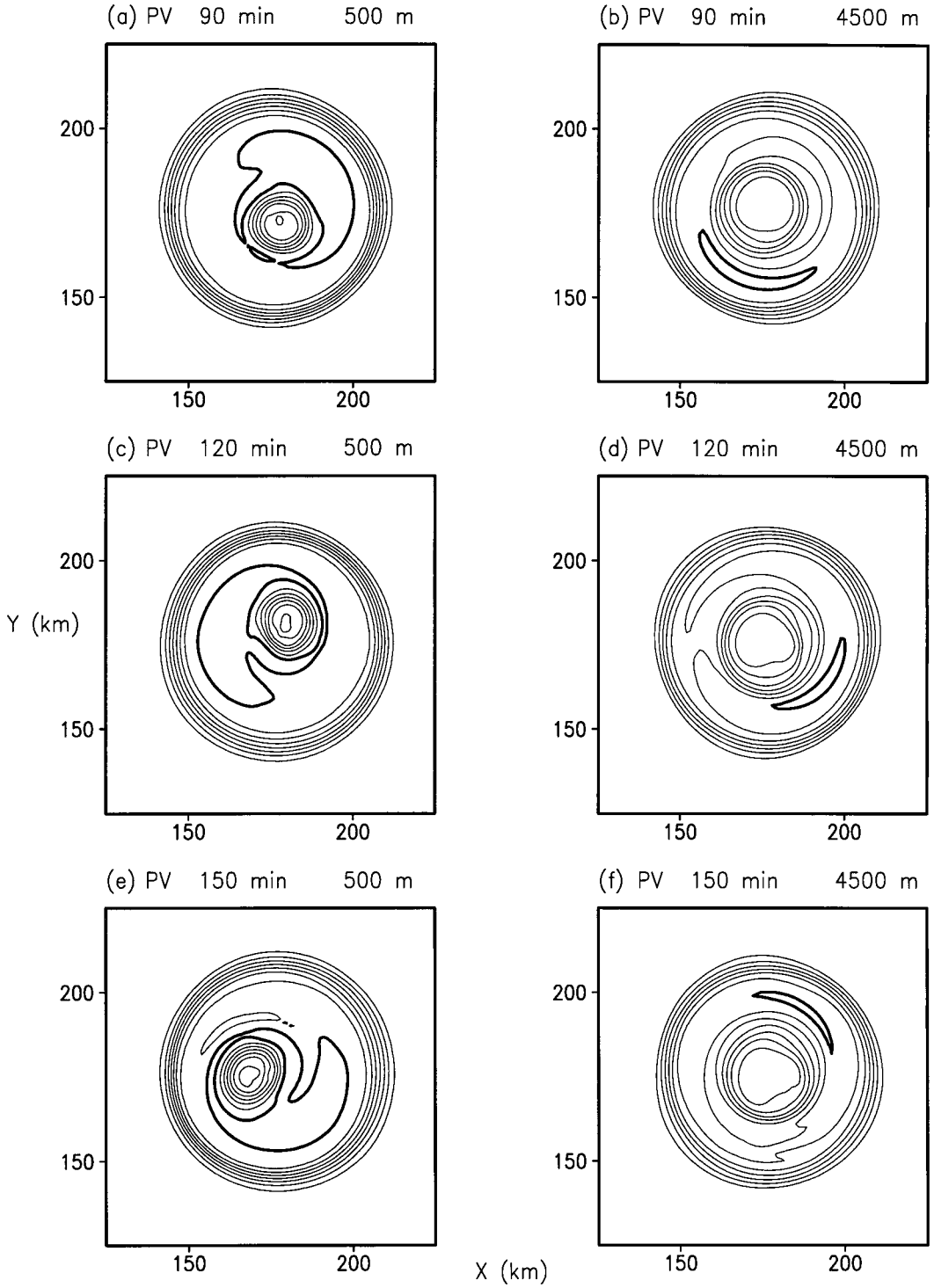

FIG. 22. Early evolution of the Ertel's PV in the mesoscale model simulation every 30 min, at $z = 0.5$ km and $z = 4.5$ km, as labeled. Contours are as in Fig. 21.

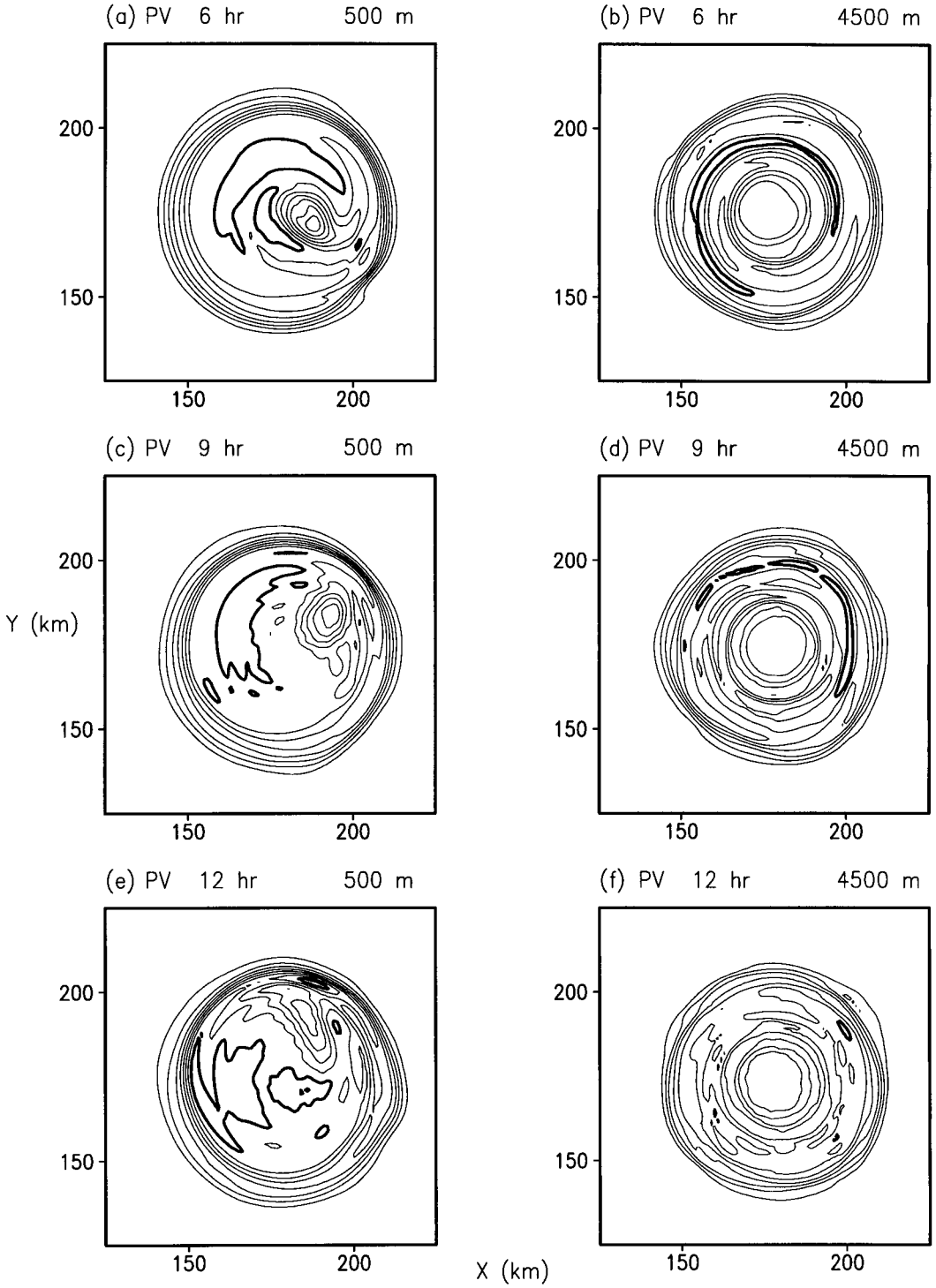

FIG. 23. Later evolution of the Ertel's PV in the mesoscale model simulation every 30 min, at $z = 0.5$ km and $z = 4.5$ km, as labeled. Contours are as in Fig. 21.

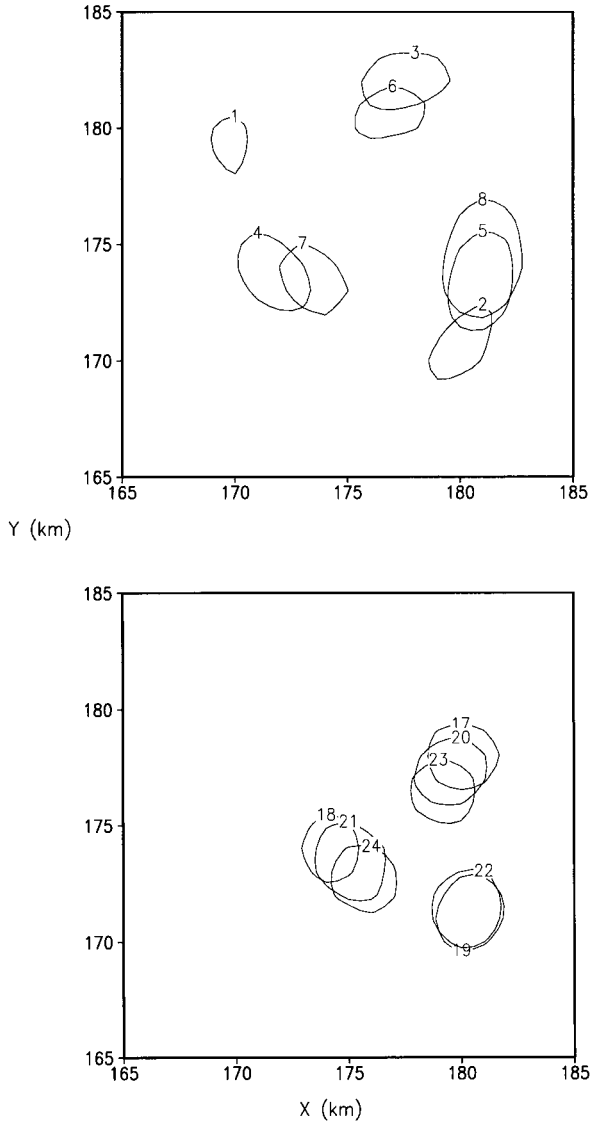

FIG. 24. The lowest contourable pressure levels at the lowest grid level (z = 500 m) in the mesoscale model simulation of the wavenumber-one instability. For each contour, the numbers indicate the time at 30-min intervals; that is, contour 1 is at t = 30 min, 2 is at t = 60 min, etc. Plot (a) shows the results for the first 8 times after t = 0, from t = 30 min to t = 4 h; the contour levels are 928.00, 927.33, 926.62, 925.74, 924.98, 924.32, 923.76, and 923.34 mb, respectively. Plot (b) shows later times, from t = 8 h 30 min to t = 12 h; the contour levels are 921.67, 921.54, 921.39, 921.24, 921.12, 921.04, 921.00, and 921.00 mb.

rapid mixing of the inner-core vorticity. Also, the wavenumber-one instability seems to be confined to the lowest few kilometers of the vortex; above, only axisymmetrization occurs. Nonetheless, the basic principle holds that a low-vorticity core, hurricane-like vortex can experience a wavenumber-one instability, and that this instability leads to inner-core vorticity mixing. Initially, the mixing proceeds due to the displacement of the low-vorticity core and a net inward flux of higher, eyewall vorticity, as was shown in the two-dimensional simulations of section 2. This mixing is later enhanced by smaller-scale, three-dimensional instabilities, which are caused by the rapidly changing horizontal and vertical structures of the PV field.

The vortices we have studied here have been constructed to be stable or at least only weakly unstable to higher wavenumber perturbations. A valid question to ask is whether or not, in the real atmosphere, the wavenumber-one instability would be dominated by higher wavenumber instabilities. Indeed, higher wavenumber instabilities in geophysical, hurricane-like, and tornado-like vortices have been a topic of considerable research (e.g., Rotunno 1978; Flierl 1988; Peng and Williams 1991; Smyth and McWilliams 1998; Schubert et al. 1999; Nolan and Farrell 1999a,b), and the authors are currently extending such work into the realm of three-dimensional, baroclinic, hurricane-like vortices similar to the vortex simulated in our mesoscale model (Nolan and Montgomery 2000b). However, the existence and relevance of the wavenumber-one instability is not precluded by higher-wavenumber dynamics. The higher wavenumber instabilities generally require that the eyewall have a certain structure—that the radius of the low-vorticity core be larger than the width of the high-vorticity eyewall annulus, and/or that the ratio of the eyewall to eye vorticity be above some value (see Schubert et al. 1999, section 2). The small amplitude, high frequency trochoidal motion of hurricanes, discussed in section 1 of this paper, is observed at least as frequently as higher-wavenumber instabilities and mesovortices within hurricanes. The wavenumber-one instability only requires the presence of an angular velocity maximum other than at the center axis, and thus can occur in hurricanes with very small eyes and also weaker storms. Furthermore, while higher-wavenumber instabilities may often be present, their smaller scales makes them less effective in ameliorating the PV maximum in the eyewall region (especially in light of the steady PV generation caused by convection) as compared to the larger displacements caused by the wavenumber-one instability (similar to the smaller total heat fluxes associated with short-wavelength baroclinic waves; see, e.g., Welch and Tung 1998).

The wavenumber-one instability presented here, and its associated trochoidal motion, are fundamentally different from the larger-scale, lower frequency trochoidal motions discussed in previous studies (e.g., Yeh 1950; Kuo 1969; Abe 1987; Flatau and Stevens 1993; Jones 1995). Rather than being caused by an interaction with the hurricane's environment, this instability is fundamental to vortices with low-vorticity cores, and represents a growing displacement of the low-vorticity center, which ultimately leads to inner-core vorticity and angular momentum redistribution. Such inner-core mixing also causes the minimum surface pressure to

fall, which may have an important impact on the further evolution of the storm.

Acknowledgments. The authors would like to thank Dr. P. Reasor for his contributions to preliminary work for this paper, and Dr. J. Kossin for his comments on the manuscript. For continuing support with the development and utilization of the Adaptive Mesh Refinement Model, the authors would also like to thank Drs. A. S. Almgren and J. B. Bell, along with the Center for Computational Sciences and Engineering and the Mathematics Department of the Lawrence Berkeley National Laboratory. This work was supported in part by the Office of Naval Research Grant N00014-93-1-0456 P0006 and Colorado State University.

APPENDIX

Neutral Inner-Core Modes in Two-Dimensional Vortices

We show that in a two-dimensional, inviscid vortex with an angular velocity maximum, a disturbance whose perturbation vorticity is exactly proportional to the basic-state vorticity gradient, up to the location of the angular velocity maximum, and zero elsewhere, is a neutral mode that rotates at the speed of the angular velocity maximum. The linearized equations of motion for inviscid perturbations are

$$\frac{\partial \zeta_n}{\partial t} + in\overline{\Omega}\zeta_n + u_n\frac{\partial \overline{\zeta}}{\partial r} = 0, \quad \text{and} \tag{A.1}$$

$$u_n = -\frac{in}{r}\psi_n, \tag{A.2}$$

where

$$\psi_n(r, t) = \int_0^R \zeta_n(\rho, t)G_n(r, \rho)\, d\rho, \tag{A.3}$$

and in a cylindrical domain of size R, the Green function for wavenumber n is

$$G_n(r, \rho) = \begin{cases} \dfrac{r^n\rho^{n+1}}{2nR^{2n}} - \dfrac{1}{2n}r^n\rho^{-n+1} & 0 \le r \le \rho \\ \dfrac{r^n\rho^{n+1}}{2nR^{2n}} - \dfrac{1}{2n}r^{-n}\rho^{n+1} & \rho \le r \le R \end{cases} \tag{A.4}$$

(Carr and Williams 1989).

Now let us consider the case for $n = 1$ and

$$\zeta_1(r, 0) = C\frac{\partial \overline{\zeta}}{\partial r}H(\mathrm{RM}\Omega - r), \tag{A.5}$$

where C is some complex constant, RMΩ is the location of the angular velocity maximum associated with the neutral mode (if there is more than one angular velocity maximum, there will be neutral modes associated with each one; see the last paragraph of this appendix), and H is the Heaviside step function. Without loss of generality we may consider the case with $C = 1$. Then how does the perturbation evolve? We must solve for the ψ_1 associated with ζ_1:

$$\begin{aligned}\psi_1(r) &= \int_0^r \frac{\partial \overline{\zeta}}{\partial \rho}\left(\frac{r\rho^2}{2R^2} - \frac{1}{2}r^{-1}\rho^2\right) d\rho \\ &\quad + \int_r^{\mathrm{RM}\Omega} \frac{\partial \overline{\zeta}}{\partial \rho}\left(\frac{r\rho^2}{2R^2} - \frac{1}{2}r\right) d\rho \\ &= \int_0^r \frac{\partial \overline{\zeta}}{\partial \rho}\left(-\frac{1}{2}r^{-1}\rho^2\right) d\rho + \int_r^{\mathrm{RM}\Omega} \frac{\partial \overline{\zeta}}{\partial \rho}\left(-\frac{1}{2}r\right) d\rho \\ &\quad + \int_0^{\mathrm{RM}\Omega} \frac{\partial \overline{\zeta}}{\partial \rho}\left(\frac{r\rho^2}{2R^2}\right) d\rho = I_1 + I_2 + I_3. \end{aligned} \tag{A.6}$$

Let us consider the first integral,

$$I_1 = -\frac{1}{2r}\int_0^r \frac{\partial \overline{\zeta}}{\partial \rho}\rho^2\, d\rho. \tag{A.7}$$

Using the definitions of vorticity and angular velocity, one can show that

$$\frac{\partial \overline{\zeta}}{\partial \rho} = \rho\frac{\partial^2 \overline{\Omega}}{\partial \rho^2} + 3\frac{\partial \overline{\Omega}}{\partial \rho}, \tag{A.8}$$

and thus

$$\rho^2\frac{\partial \overline{\zeta}}{\partial \rho} = \frac{\partial}{\partial \rho}\left(\rho^3\frac{\partial \overline{\Omega}}{\partial \rho}\right). \tag{A.9}$$

Therefore,

$$\begin{aligned} I_1 &= -\frac{1}{2r}\int_0^r \frac{\partial}{\partial \rho}\left(\rho^3\frac{\partial \overline{\Omega}}{\partial \rho}\right) d\rho = -\frac{1}{2}r^2\frac{\partial \overline{\Omega}}{\partial r} \\ &= \frac{1}{2}\overline{v} - \frac{r}{2}\frac{\partial \overline{v}}{\partial r}. \end{aligned} \tag{A.10}$$

Using (A.9), we can write the third integral as

$$I_3 = \frac{r}{2R^2}\int_0^{\mathrm{RM}\Omega} \frac{\partial}{\partial \rho}\left(\rho^3\frac{\partial \overline{\Omega}}{\partial \rho}\right) d\rho = 0, \tag{A.11}$$

even for finite R, due to the definition of RMΩ. We now proceed with the second integral,

$$\begin{aligned} I_2 &= -\frac{1}{2}r\int_r^{\mathrm{RM}\Omega} \frac{\partial \overline{\zeta}}{\partial \rho}\, d\rho \\ &= -\frac{1}{2}r[\overline{\zeta}(\mathrm{RM}\Omega) - \overline{\zeta}(r)]. \end{aligned} \tag{A.12}$$

Since $\overline{\zeta} = \partial\overline{v}/\partial r + \overline{v}/r$, we can rewrite I_2 as

$$I_2 = -\frac{1}{2}r\left[\left(\frac{\partial\overline{v}}{\partial r} + \frac{\overline{v}}{r}\right)_{r=\mathrm{RM}\Omega} - \left(\frac{\partial\overline{v}}{\partial r} + \frac{\overline{v}}{r}\right)\right]. \quad \text{(A.13)}$$

The final step is to use the identity

$$\left(\frac{\partial\overline{v}}{\partial r}\right)_{r=\mathrm{RM}\Omega} = \left(\overline{\Omega} + r\frac{\partial\overline{\Omega}}{\partial r}\right)_{r=\mathrm{RM}\Omega} = \overline{\Omega}_{\max}, \quad \text{(A.14)}$$

so that we may arrive at the solution

$$\psi_1(r) = I_1 + I_2 = r[\overline{\Omega}(r) - \overline{\Omega}_{\max}]. \quad \text{(A.15)}$$

In fact, (A.15) only applies for $r \le \mathrm{RM}\Omega$; for $r > \mathrm{RM}\Omega$, $\psi_1(r) = I_1(r) = I_1(\mathrm{RM}\Omega) = 0$.

Now, if we substitute (A.5) and (A.15) into (A.1) and (A.2), we arrive at the equation of motion

$$\frac{\partial\zeta_1}{\partial t} + i\overline{\Omega}_{\max}\zeta_1 = 0; \quad \text{(A.16)}$$

that is, the perturbation has fixed structure and rotates at the maximum angular velocity.

Finally, we note that these arguments do not rely on the uniqueness of the angular velocity maximum. That is to say, for a vortex with an arbitrary number of angular velocity maxima, there will be a neutral mode associated with each maximum. The arguments above will apply in each case, provided that the RMΩ used throughout is the same as that in (A.5). As SR showed in their original solution, there will also be an algebraic instability associated with each of the angular velocity maxima.

REFERENCES

Abe, S., 1987: The looping motion and asymmetry of tropical cyclone. *J. Meteor. Soc. Japan*, **65,** 247–257.

Almgren, A. S., J. B. Bell, P. Colella, L. H. Howell, and M. L. Welcome, 1998: A conservative adaptive projection method for the variable density incompressible Navier–Stokes equations. *J. Comput. Phys.*, **142,** 1–46.

Braun, S. A., and W.-K. Tao, 2000: Sensitivity of high-resolution simulations of Hurricane Bob (1991) to planetary boundary layer parameterizations. *Mon. Wea. Rev.*, **128,** 3941–3961.

——, J. Simpson, and W.-K. Tao, 2000: Kinematic and thermodynamics structures of Hurricane Bob (1991) determined from a 1.3 km resolution numerical simulation. Preprints, *24th Conf. on Hurricanes and Tropical Meteorology*, Fort Lauderdale, FL, Amer. Meteor. Soc., 376–377.

Carr, L. E., III, and R. T. Williams, 1989: Barotropic vortex stability to perturbations from axisymmetry. *J. Atmos. Sci.*, **46,** 3177–3191.

Chen, Y., and M. K. Yau, 2001: Spiral bands in a simulated hurricane. Part I: Vortex Rossby wave verification. *J. Atmos. Sci.*, **58,** 2128–2145.

Daida, S. K., and G. M. Barnes, 2000: The eyewall of category 1 Hurricane Paine near landfall. Preprints, *24th Conf. on Hurricanes and Tropical Meteorology*, Fort Lauderdale, FL, Amer. Meteor. Soc., 414–415.

Dodge, P., R. W. Burpee, and F. D. Marks Jr., 1999: The kinematic structure of a hurricane with sea level pressure less than 900 mb. *Mon. Wea. Rev.*, **127,** 987–1004.

Driscoll, C. F., 1990: Observations of an unstable $l = 1$ diocotron mode on a hollow electron column. *Phys. Rev. Lett.*, **64,** 645–648.

——, K. S. Fine, X.-P. Huang, T. B. Mitchell, and B. P. Cluggish, 1996: Vortices and turbulent relaxation in magnetized electron columns. *Transp. Chaos Plasma Phys.*, **2,** 19–38.

Emanuel, K. E., 1997: Some aspects of hurricane inner-core dynamics and energetics. *J. Atmos. Sci.*, **54,** 1014–1026.

Finn, J. M., D. del-Castillo-Negrete, and D. C. Barnes, 1999a: Compressional effects in non-neutral plasmas, a shallow water analogy and $m = 1$ instability. *Phys. Plasmas*, **6,** 3744–3758.

——, ——, and ——, 1999b: Destabilization of the $m = 1$ diocotron mode in non-neutral plasmas. *Phys. Rev. Lett.*, **84,** 2401–2404.

Flatau, M., and D. E. Stevens, 1989: Barotropic and inertial instabilities in the hurricane outflow layer. *Geophys. Astrophys. Fluid Dyn.*, **47,** 1–18.

——, and ——, 1993: The role of outflow-layer instabilities in tropical cyclone motion. *J. Atmos. Sci.*, **50,** 1721–1733.

——, W. H. Schubert, and D. E. Stevens, 1994: The role of baroclinic processes in tropical cyclone motion: The influence of vertical tilt. *J. Atmos. Sci.*, **51,** 2589–2601.

Flierl, G. R., 1988: On the instability of geostrophic vortices. *J. Fluid Mech.*, **197,** 349–388.

Fulton, J. D., M. T. Montgomery, and S. A. Braun, 2000: Vortex Rossby waves and vorticity mixing in a MM5 simulation of Hurricane Bob (1991). Preprints, *24th Conf. on Hurricanes and Tropical Meteorology*, Fort Lauderdale, FL, Amer. Meteor. Soc., 374–375.

Griffin, J. S., R. W. Burpee, F. D. Marks Jr., and J. L. Franklin, 1992: Real-time airborne analysis of aircraft data supporting operational hurricane forecasting. *Wea. Forecasting*, **7,** 480–490.

Huang, X.-P., K. S. Fine, and C. F. Driscoll, 1995: Coherent vorticity holes from 2D turbulence decaying in a background shear flow. *Phys. Rev. Lett.*, **74,** 4424–4427.

Jarvinen, B. R., C. J. Neumann, and M. A. S. Davis, 1984: A tropical cyclone data tape for the North Atlantic basic, 1886–1983: Contents, limitations, and uses. NOAA Tech. Memo. NWS NHC 22, 21 pp.

Jones, R. W., 1977: Vortex motion in a tropical cyclone model. *J. Atmos. Sci.*, **34,** 1518–1527.

Jones, S. C., 1995: The evolution of vortices in vertical shear. I: Initially barotropic vortices. *Quart. J. Roy. Meteor. Soc.*, **121,** 821–851.

Jordan, C. L., 1958: Mean soundings for the West Indies area. *J. Meteor.*, **15,** 91–97.

——, 1966: Surface pressure variations at coastal stations during the period of irregular motion of Hurricane Carla of 1961. *Mon. Wea. Rev.*, **94,** 454–458.

Jordan, H. M., and D. J. Stowell, 1955: Some small scale features of the track of Hurricane Ione. *Mon. Wea. Rev.*, **83,** 210–215.

Klemp, J. B., and R. B. Wilhemson, 1978: The simulation of three-dimensional covective storm dynamics. *J. Atmos. Sci.*, **35,** 1070–1096.

Kossin, J. P., and M. D. Eastin, 2001: Two distinct regimes in the kinematic and thermodynamic structure of the hurricane eye and eyewall. *J. Atmos. Sci.*, **58,** 1079–1090.

——, W. S. Schubert, and M. T. Montgomery, 2000: Unstable interactions between a hurricane's primary eyewall and a secondary ring of enhanced vorticity. *J. Atmos. Sci.*, **57,** 3893–3917.

Kuo, H., 1950: The motion of atmospheric vortices and the general circulations. *J. Meteor.*, **7,** 247–258.

——, 1969: Motions of vortices and circulating cylinder in shear flow with friction. *J. Atmos. Sci.*, **26,** 390–398.

Lamb, H., 1932: *Hydrodynamics.* Dover, 738 pp.

Lawrence, M. B., and B. M. Mayfield, 1977: Satellite observations of trochoidal motion during Hurricane Belle 1976. *Mon. Wea. Rev.*, **105,** 1458–1461.

Lilly, D. K., 1962: On the numerical simulation of bouyant convection. *Tellus*, **14,** 148–172.

Liu, Y., D.-L. Zhang, and M. K. Yau, 1997: A multiscale numerical study of Hurricane Andrew (1992). Part I: An explicit simulation. *Mon. Wea. Rev.*, **125,** 3073–3093.

——, ——, and ——, 1999: A multiscale numerical study of Hur-

ricane Andrew (1992). Part II: Kinematics and inner-core structures. *Mon. Wea. Rev.,* **127,** 2597–2616.
Marks, F. D., 1992: Kinematic structure of the hurricane inner core as revealed by airborne Doppler radar. Preprints, *Fifth Conf. on Mesoscale Processes,* Atlanta, GA, Amer. Meteor. Soc., 127–132.
McWilliams, J. C., 1985: A uniformly valid model spanning the regimes of geostrophic and isotropic, stratified turbulence: Balanced turbulence. *J. Atmos. Sci.,* **42,** 1773–1774.
Möller, J. D., and M. T. Mongomery, 2000: Tropical cyclone evolution via potential vorticity anomalies in a three-dimensional balance model. *J. Atmos. Sci.,* **57,** 3366–3386.
Montgomery, M. T., and R. J. Kallenbach, 1997: A theory for vortex Rossby waves and its application to spiral bands and intensity changes in hurricanes. *Quart. J. Roy. Meteor. Soc.,* **123,** 435–465.
——, and C. Lu, 1997: Free waves on barotropic vortices. Part I: Eigenmode structure. *J. Atmos. Sci.,* **54,** 1868–1885.
——, and J. L. Franklin, 1998: An assesment of the balance approximation in hurricanes. *J. Atmos. Sci.,* **55,** 2193–2200.
——, J. D. Möller, and C. T. Nicklas, 1999: Linear and nonlinear vortex motion in an asymmetric balance shallow water model. *J. Atmos. Sci.,* **56,** 749–768.
Muramatsu, T., 1986: Trochoidal motion of the eye of Typhoon 8019. *J. Meteor. Soc. Japan,* **64,** 259–272.
Nolan, D. S., and B. F. Farrell, 1999a: Generalized stability analyses of asymmetric disturbances in one- and two-celled vortices maintained by radial inflow. *J. Atmos. Sci.,* **56,** 1282–1307.
——, and ——, 1999b: The intensification of two-dimensional swirling flows by stochastic asymmetric forcing. *J. Atmos. Sci.,* **56,** 3937–3962.
——, and M. T. Montgomery, 2000a: The algebraic growth of wavenumber one disturbances in hurricane-like vortices. *J. Atmos. Sci.,* **57,** 3514–3538.
——, and ——, 2000b: Three-dimensional, asymmetric, nonhydrostatic, unstable eigenmodes in balanced, hurricane-like vortices. Preprints, *24th Conf. on Hurricanes and Tropical Meteorology,* Fort Lauderdale, FL, Amer. Meteor. Soc., 163–164.
——, A. S. Almgren, and J. B. Bell, 2000: Studies of the relationship between the structure and dynamics of tornado-like vortices and their environmental forcing. Lawrence Berkeley National Laboratory Rep. LBNL-47554, 65 pp.
Pedlosky, J., 1987: *Geophysical Fluid Dynamics.* Springer-Verlag, 710 pp.
Peng, M. S., and R. T. Williams, 1991: Stability analyses of barotropic vortices. *Geophys. Astrophys. Fluid Dyn.,* **58,** 263–283.
Pielke, R. A., and Coauthors, 1992: A comprehensive meteorological modeling system—RAMS. *Meteor. Atmos. Phys.,* **49,** 69–91.
Raymond, D. J., 1992: Nonlinear balance and potential vorticity thinking at large Rossby number. *Quart. J. Roy. Meteor. Soc.,* **118,** 987–1015.
Reasor, P. D., and M. T. Montgomery, 2001: Three-dimensional alignment and corotation of weak, TC-like vortices via linear vortex Rossby waves. *J. Atmos. Sci.,* **58,** 2306–2330.
——, ——, F. D. Marks, and J. F. Gamache, 2000: Low-wavenumber structure and evolution of the hurricane inner core observed by airborne dual-Doppler radar. *Mon. Wea. Rev.,* **128,** 1653–1680.
Reznik, G. M., and W. K. Dewar, 1994: An analytical theory of distributed axisymmetric barotropic vortices on the beta-plane. *J. Fluid Mech.,* **269,** 301–321.
Rotunno, R., 1978: A note on the stability of a cylindrical vortex sheet. *J. Fluid Mech.,* **87,** 761–771.
Roux, F., and N. Viltard, 1995: Structure and evolution of Hurricane Claudette on 7 September 1991 from airborne Doppler radar observation. Part I: Kinematics. *Mon. Wea. Rev.,* **123,** 2611–2639.
Schecter, D. A., and D. H. E. Dubin, 1999: Vortex motion driven by a background vorticity gradient. *Phys. Rev. Lett.,* **83,** 2191–2194.
——, ——, K. S. Fine, and C. F. Driscoll, 1999: Vortex crystals from 2D euler flow: Experiment and simulation. *Phys. Fluids,* **11,** 905–912.
Schubert, W. H., M. T. Montgomery, R. K. Taft, T. G. Guinn, S. R. Fulton, J. P. Kossin, and J. P. Edwards, 1999: Polygonal eyewalls, asymmetric eye contraction, and potential vorticity mixing in hurricanes. *J. Atmos. Sci.,* **56,** 1197–1223.
Shapiro, L. J., and M. T. Montgomery, 1993: A three-dimensional balance theory for rapidly rotating vortices. *J. Atmos. Sci.,* **50,** 3322–3335.
Shea, D. J., and W. H. Gray, 1973: The hurricane's inner core region. I: Symmetric and asymmetric structure. *J. Atmos. Sci.,* **30,** 1544–1564.
Smagorinsky, J., 1963: General circulation experiments with the primitive equations. Part I: The basic experiment. *Mon. Wea. Rev.,* **91,** 99–164.
Smith, R. A., and M. N. Rosenbluth, 1990: Algebraic instability of hollow electron columns and cylindrical vortices. *Phys. Rev. Lett.,* **64,** 649–652.
Smith, R. K., and H. C. Weber, 1993: An extended analytic theory of tropical cyclone motion in a barotropic shear flow. *Quart. J. Roy. Meteor. Soc.,* **121,** 15 615–15 650.
Smyth, W. D., and J. C. McWilliams, 1998: Instability of an axisymmetric vortex in a stably stratified, rotating environment. *Theor. Comput. Fluid Dyn.,* **11,** 305–322.
Tripoli, G. J., and W. R. Cotton, 1982: The Colorado State University three-dimensional cloud mesoscale model, 1982. Part I: General theoretical framework and sensitivity experiments. *J. Rech. Atmos.,* **16,** 185–220.
Welch, W. T., and K. K. Tung, 1998: On the equilibrium spectrum of transient waves in the atmosphere. *J. Atmos. Sci.,* **55,** 2833–2851.
Willoughby, H. E., 1992: Linear motion of a shallow-water barotropic vortex as an initial value problem. *J. Atmos. Sci.,* **49,** 2015–2031.
——, F. D. Marks Jr., and R. J. Feinberg, 1984: Stationary and moving convective bands in hurricanes. *J. Atmos. Sci.,* **41,** 3189–3211.
Wu, C.-C., and K. E. Emanuel, 1993: Interaction of a baroclinic vortex with background shear: Application to hurricane movement. *J. Atmos. Sci.,* **50,** 62–76.
Yeh, T. C., 1950: The motion of tropical storms under the influence of a superimposed southerly current. *J. Meteor.,* **7,** 108–113.